Analytic theory for betatron radiation from relativistic electrons in ion plasma channels with magnetic field

H. C. Lee and T. F. Jiang

Articles you may be interested in

Nonlinear Zakharov–Kuznetsov equation for obliquely propagating two-dimensional ion-acoustic solitary waves in a relativistic, rotating magnetized electron-positron-ion plasma
Phys. Plasmas **12**, 072306 (2005); 10.1063/1.1946729

Simulations and theories of relativistic ion cyclotron instabilities driven by MeV alpha particles in thermal deuterium plasmas
Phys. Plasmas **10**, 1315 (2003); 10.1063/1.1561611

Relativistic electromagnetic solitons in a warm quasineutral electron–ion plasma
Phys. Plasmas **10**, 639 (2003); 10.1063/1.1544666

Generation of magnetic field and electrostatic shock wave driven by counterstreaming pair plasmas
Phys. Plasmas **10**, 392 (2003); 10.1063/1.1540095

Ion acceleration, magnetic field line reconnection, and multiple current filament coalescence of a relativistic electron beam in a plasma
Phys. Plasmas **9**, 2959 (2002); 10.1063/1.1484156

Analytic theory for betatron radiation from relativistic electrons in ion plasma channels with magnetic field

H. C. Lee[a)] and T. F. Jiang
Institute of Physics, National Chiao Tung University, Hsinchu 30010, Taiwan

We analytically solve the relativistic equation of motion for an electron in ion plasma channels and calculate the corresponding trajectory as well as the synchrotron radiation. The relativistic effect on a trajectory is strong, i.e., many high-order harmonic terms in the trajectory, when the ratio of the initial transverse velocity (v_{x0}) to the longitudinal velocity (v_{z0}) of the electron injected to ion plasma channels is high. Interestingly, these high-order harmonic terms result in a quite broad and intense radiation spectrum, especially at an oblique angle, in contrast to an earlier understanding. As the initial velocity ratio ($v_{x0}:v_{z0}$) decreases, the relativistic effect becomes weak; only the first and second harmonic terms remain in the transverse and longitudinal trajectories, respectively, which coincides with the result of Esarey *et al.* [Phys. Rev. E **65**, 056505 (2002)]. Our formalism also allows the description of electron's trajectory in the presence of an applied magnetic field. Critical magnetic fields for cyclotron motions are figured out and compared with semiclassical results. The cyclotron motion leads to more high-order harmonic terms than the trajectory without magnetic fields and causes an immensely broad spectrum with vastly large radiation amplitude for high initial velocity ratios ($v_{x0}:v_{z0}$). The radiation from hard x-ray to gamma-ray regions can be generated with a broad radiation angle, thus available for applications. © *2010 American Institute of Physics.* [doi:10.1063/1.3496983]

I. INTRODUCTION

The emergence of ultraintense laser pulses generated by the chirped pulse amplification[1] has made it possible to obtain beam intensities higher than 10^{18} W/cm^2 and results in considerable applications, such as laser-driven plasma-based (LDPB) accelerators[2–5] as well as high-order harmonic generation[6–10] leading to attosecond pulses[11–13] and femtosecond x-ray sources.[14,15] The LDPB accelerator is particularly interesting for its extremely high accelerating electric field[2–4,16–19] >100 GV/m, which is approximately three orders of magnitude greater than that obtained by radio-frequency linear accelerators.[20] Currently, high-quality electron bunches up to an order of GeV were experimentally demonstrated.[16] The centimeter accelerating distance makes relative experiments shrink to a tabletop scale. The plasma wave, which sustains an ultrahigh accelerated field, is excited due to the ponderomotive force[5] ($-m_ec^2\nabla\gamma$) when the ultraintense laser pulse is focused into a gas jet, where m_e, c, and γ are the electron rest mass, the speed of light, and the Lorentz factor, respectively. An electron trapped by the plasma wave thus accelerates. Furthermore, the ponderomotive force drives untrapped electrons away from the strong field region, thus leaving an ion cavity almost free from background electrons if the laser intensity is strong enough, i.e., the blow-out regime.[21,22] The ion cavity acts as a space-charge region and gives the accelerated electron a restoring force. Due to the restoring force, the accelerated electron undergoes an oscillation, also called betatron oscillation,[23,24] although no magnetic undulators are used, and synchrotron

radiation is emitted.[14,25–34] The radiation frequency of the betatron oscillation can reach the hard x-ray region. Several groups have experimentally demonstrated the fact. Until now, the highest photon energy due to betatron oscillation can reach 50 keV, to the best of our knowledge.[35]

On the theoretical side, the radiation can be calculated via the Liénard–Wiechert potentials,[36] according to its electron's trajectory determined by using the relativistic equation of motion[25–28,30–32] or the particle in cell (PIC) code.[14,29,33,35] Due to the Lorentz factor, the relativistic equation is highly nonlinear, and an analytic solution is difficult to obtain. Therefore, a semiclassical approximation is often made in the equation of motion,[27,28,30–32] where $d\gamma/dt$ is neglected, and hence the equation is classical except the relativistic mass. However, the approximation may lose higher-order harmonic terms in the electron's trajectory and thus underestimates the width of the radiation spectrum. Esarey *et al.*[25] figured out this point and showed that the electron's longitudinal orbit $z(t)$ has a second harmonic oscillation term $\sin(2\omega_\beta t)$, in addition to a first harmonic term $\sin(\omega_\beta t)$ in the transverse orbit $x(t)$ when no magnetic field is applied, where ω_β is the betatron frequency defined later. In this paper, we analytically solve the relativistic equation of motion to obtain the exact trajectory of the betatron oscillation, which is used to calculate synchrotron radiation. We find that the second harmonic term indeed exists and is unique in the $z(t)$ when the ratio of the initial transverse velocity (v_{x0}) to the longitudinal velocity (v_{z0}) of the electron injected to the ion plasma channel is low. However, as the initial velocity ratio ($v_{x0}:v_{z0}$) increases, other higher-order harmonic terms are excited, leading to a quite broad and intense radiation spectrum, especially at an oblique angle, in contrast to an earlier

a)Author to whom correspondence should be addressed. Electronic mail: hclee@mail.nctu.edu.tw.

understanding that the strongest radiation appears on the axis ($\theta=0$). Hence, in the later case (high initial velocity ratio $v_{x0}:v_{z0}$), a fully relativistic calculation is needed.

The performance of electrons before undergoing betatron oscillation strongly depends on the stage during propagation of ultraintense laser pulse in plasma channels. Applying a magnetic field was recently shown to enhance guiding laser pulse in LDPB accelerators to overcome the dephasing effect for gaining higher electron's energy[37] and to improve electron beam's quality about narrower energy spreading bunches.[38] On the other hand, a spontaneous short-pulsed (picoseconds) magnetic field of the order of megagauss is generated during the laser-plasma interaction due to the inverse Faraday effect (both circularly[39,40] and linearly[41,42] polarizations) or gradient of density and temperature in plasma.[43] The inducing magnetic field will then influence the plasma dynamics and have important effects on LDPB accelerators and inertial confinement fusion.[44] While magnetic fields manifest much importance on intense-field physics, the betatron radiation subject to an external magnetic field has not been rigorously studied yet. Our formalism for betatron oscillation allows the presence of a magnetic field. Thus, an analytic relativistic trajectory can be demonstrated. We find that the cyclotron motion is significant in radiation spectra. Due to its rich high-order harmonic terms, the betatron oscillation with a high initial velocity ratio ($v_{x0}:v_{z0}$) can emit an immensely broad radiation spectrum, at least 10^7 times the betatron frequency, together with a vastly large amplitude. The radiation can easily go beyond the hard x-ray region (12–120 keV) and extend to the gamma-ray region. Due to the importance of cyclotron motions, a set of conditions for critical magnetic fields is presented and the generation of the required magnetic fields is discussed.

The rest of this paper is organized as follows. We derive the analytic trajectory for the relativistic equation of motion in Sec. II A and synchrotron radiation for corresponding trajectories in Sec. II B. We show the results and discussions for trajectories in Sec. III A and for the radiation spectrum with a detailed angular dependence in Sec. III B. Conclusions are finally drawn in Sec. IV.

II. THEORY

A. Trajectory

The relativistic equation of motion for an electron in the ion plasma channel with an applied magnetic field $\mathbf{B}_0$ and an additional electric field $\mathbf{E}_0$ can be expressed as

$$\mathbf{F} = m_e\frac{d(\gamma\mathbf{v})}{dt} = -k_r\mathbf{x}_\perp + q(\mathbf{E}_0 + \mathbf{v}\times\mathbf{B}_0), \quad (1)$$

where the restoring strength k_r equals[25–28,30,32] $m_e\omega_p^2/2$ with the plasma frequency $\omega_p=\sqrt{n_pe^2/m_e\varepsilon}$. n_p is the plasma density and ε is the dielectric constant. $\mathbf{x}_\perp$ denotes the transverse (x,y) trajectory. The coordinate is shown in Fig. 1. For simplicity, the initial y-component velocity (v_{y0}) is set to zero, and thus the electron's motion lies on the x-z plane. $\mathbf{B}_0$ is parallel to the y axis. The relativistic derivation also allows a field $\mathbf{E}_0$ parallel to the x axis, which can generate an $\mathbf{E}_0\times\mathbf{B}_0$ drift (or acceleration[45]) as a possible application in
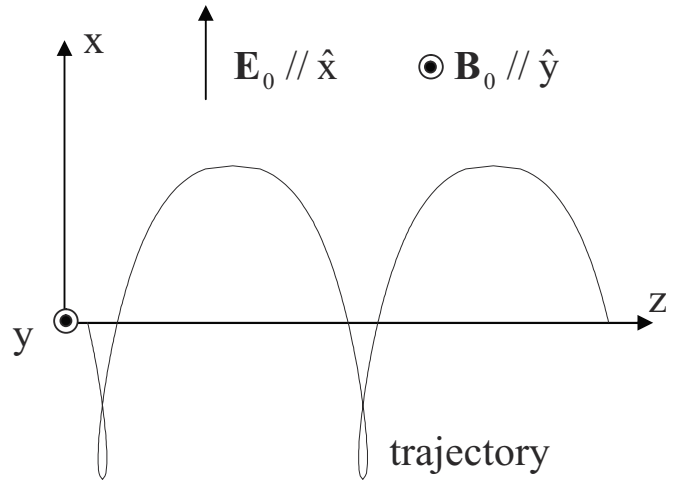

FIG. 1. Schematic diagram for an electron in an ion plasma channel subject to an electric field and a magnetic field.

the future. After some substitutions, Eq. (1) and its energy equation calculated by $d(m_e\gamma c^2)/dt=\mathbf{F}\cdot\mathbf{v}$ can then be presented as

$$m_e\frac{d(\gamma v_x)}{dt} = -k_rx + qE_0 - qB_0v_z, \quad (2)$$

$$m_e\frac{d(\gamma v_z)}{dt} = qB_0v_x, \quad (3)$$

$$m_ec^2\frac{d\gamma}{dt} = (-k_rx + qE_0)v_x. \quad (4)$$

Integrating Eqs. (3) and (4) with respect to time yields

$$\gamma v_z - \gamma_0 v_{z0} = \omega_c(x - x_0), \quad (5)$$

$$m_e\gamma c^2 + \tfrac{1}{2}k_rx^2 - qE_0x = m_e\gamma_0c^2 + \tfrac{1}{2}k_rx_0^2 - qE_0x_0, \quad (6)$$

respectively, where γ_0 is the initial Lorentz factor. x_0 denotes the initial x position, i.e., $x(t=0)$, and is assumed to be zero in this report. The cyclotron frequency ω_c is equal to qB_0/m_e.

Substituting the Lorentz factor into Eq. (5) and taking some arrangements yield

$$v_z^2 = \frac{(\gamma_0v_{z0} + \omega_cx)^2}{1 + (\gamma_0v_{z0} + \omega_cx)^2/c^2}\left(1 - \frac{v_x^2}{c^2}\right) = \alpha(x)\left(1 - \frac{v_x^2}{c^2}\right), \quad (7)$$

where $\alpha(x)=(\gamma_0v_{z0} + \omega_cx)^2/[1 + (\gamma_0v_{z0} + \omega_cx)^2/c^2]$.

Inputting Eq. (7) into Eq. (6) with some arrangements and scaling variables yield

$$\frac{d\tilde{x}}{dt} = \pm\sqrt{1 - \frac{1 + \left(\dfrac{\gamma_0v_{z0}}{c} + \omega_c\tilde{x}\right)^2}{\left(\gamma_0 + \tilde{E}_0\tilde{x} - \tfrac{1}{2}\omega_r^2\tilde{x}^2\right)^2}}, \quad (8)$$

where $\tilde{x}=x/c$, $\tilde{E}_0=qE_0/m_ec$, and $\omega_r=\sqrt{k_r/m_e}$.

By solving Eq. (8), we can obtain

$$t(\widetilde{x}) = \int_0^{\widetilde{x}} \frac{\left(\gamma_0 + \widetilde{E}_0 \widetilde{x}' - \frac{1}{2}\omega_r^2 \widetilde{x}'^2\right) d\widetilde{x}'}{\sqrt{\left(\gamma_0 + \widetilde{E}_0 \widetilde{x}' - \frac{1}{2}\omega_r^2 \widetilde{x}'^2\right)^2 - 1 - \left(\frac{\gamma_0 v_{z0}}{c} + \omega_c \widetilde{x}'\right)^2}}.$$

(9)

In the absence of E_0 and B_0 fields, Eq. (9) can be written in an analytic form as

$$t(\widetilde{x}) = \int_0^{\widetilde{x}} \frac{\left(\gamma_0 - \frac{1}{2}\omega_r^2 \widetilde{x}'^2\right) d\widetilde{x}'}{\sqrt{\left(\gamma_0 - \frac{1}{2}\omega_r^2 \widetilde{x}'^2\right)^2 - \left(\frac{1}{\sqrt{1-\widetilde{\alpha}_0}}\right)^2}}$$

$$= \int_0^{\widetilde{x}} \frac{\left(\frac{2\gamma_0}{\omega_r^2} - \widetilde{x}'^2\right) d\widetilde{x}'}{\sqrt{(a^2 - \widetilde{x}'^2)(b^2 - \widetilde{x}'^2)}}$$

$$= -\frac{2}{a\omega_r^2 \sqrt{1-\widetilde{\alpha}_0}} F(\theta, \eta) + aE(\theta, \eta),$$

(10)

where $\widetilde{\alpha}_0 = (\gamma_0 v_{z0})^2 / [c^2 + (\gamma_0 v_{z0})^2]$, $a = \sqrt{2}\omega_r^{-1}\sqrt{\gamma_0 + 1/\sqrt{1-\widetilde{\alpha}_0}}$, $b = \sqrt{2}\omega_r^{-1}\sqrt{\gamma_0 - 1/\sqrt{1-\widetilde{\alpha}_0}}$, $\eta = b/a$, and $\theta = \sin^{-1}(\widetilde{x}/b)$. $F(\theta,\eta) = \int_0^\theta du / \sqrt{1 - \eta^2 \sin^2 u}$ and $E(\theta,\eta) = \int_0^\theta du \sqrt{1 - \eta^2 \sin^2 u}$ are the elliptic integrals of the first and second kinds,[46] respectively.

The integral range of Eq. (9) is determined by $\widetilde{x}_{max}$ and $\widetilde{x}_{min}$. They can be found by setting Eq. (8) to zero, which results in the following quartic equation:

$$\widetilde{x}^4 - 4\frac{\widetilde{E}_0}{\omega_r^2}\widetilde{x}^3 + \frac{4}{\omega_r^4}(\widetilde{E}_0 - \gamma_0 \omega_r^2 - \omega_c^2)\widetilde{x}^2$$

$$+ \frac{8\gamma_0}{\omega_r^4}\left(\widetilde{E}_0 - \frac{\omega_c v_{z0}}{c}\right)\widetilde{x} + \frac{4}{\omega_r^4}\left(\gamma_0^2 - \frac{1}{1-\widetilde{\alpha}_0}\right) = 0.$$

(11)

In the absence of E_0 and B_0 fields, the solution of Eq. (11) is easily found,

$$\widetilde{x}_{max(min)} = \pm \frac{\sqrt{2}}{\omega_r}\sqrt{\gamma_0 - \frac{1}{\sqrt{1-\widetilde{\alpha}_0}}}.$$

(12)

In the presence of the external fields, Eq. (11) can also be exactly solved. Because the analytic solution has a complicated expression with an amount of parameters' definition, we leave the result together with its derivation in the Appendix.

Once x_{max} and x_{min} are known, the transverse trajectory $x(t)$ can be calculated by Eq. (9). Now, we turn to find the longitudinal trajectory. From Eq. (7), we can obtain

$$\frac{dz}{dt} = \pm \sqrt{\alpha(x)}\sqrt{\left[1 - \frac{1}{c^2}\left(\frac{dx}{dt}\right)^2\right]}.$$

(13)

Multiplying dt/dx in both sides of Eq. (13) and scaling variables, then yield

$$\frac{d\widetilde{z}}{d\widetilde{x}} = \pm \sqrt{\widetilde{\alpha}(\widetilde{x})}\sqrt{\left(\frac{dt}{d\widetilde{x}}\right)^2 - 1},$$

(14)

where $\widetilde{z} = z/c$ and $\widetilde{\alpha}(\widetilde{x}) = \alpha(x)/c^2$.

The differential $dt/d\widetilde{x}$ can be obtained by Eq. (9). Substituting it into Eq. (14) yields

$$\frac{d\widetilde{z}}{d\widetilde{x}} = \pm \frac{\frac{\gamma_0 v_{z0}}{c} + \omega_c \widetilde{x}}{\sqrt{\left(\gamma_0 + \widetilde{E}_0 \widetilde{x} - \frac{1}{2}\omega_r^2 \widetilde{x}^2\right)^2 - 1 - \left(\frac{\gamma_0 v_{z0}}{c} + \omega_c \widetilde{x}\right)^2}}.$$

(15)

By solving Eq. (15), we can get the longitudinal trajectory $\widetilde{z}$ in terms of $\widetilde{x}$,

$$\widetilde{z}(\widetilde{x}) = \int_0^{\widetilde{x}} \frac{\left(\frac{\gamma_0 v_{z0}}{c} + \omega_c \widetilde{x}'\right) d\widetilde{x}'}{\sqrt{\left(\gamma_0 + \widetilde{E}_0 \widetilde{x}' - \frac{1}{2}\omega_r^2 \widetilde{x}'^2\right)^2 - 1 - \left(\frac{\gamma_0 v_{z0}}{c} + \omega_c \widetilde{x}'\right)^2}},$$

(16)

where the initial condition of $\widetilde{z}(\widetilde{x}=0)=0$ is assumed.

In the absence of E_0 and B_0 fields, Eq. (16) can be written in an analytic form as

$$\widetilde{z}(\widetilde{x}) = \frac{2}{a\omega_r^2}\sqrt{\frac{\widetilde{\alpha}_0}{1-\widetilde{\alpha}_0}}F(\theta, \eta).$$

(17)

For comparison, the analytic semiclassical trajectory is also shown. Neglecting the term $d\gamma/dt$ in Eq. (1) yields the semiclassical equation of motion as

$$m_e \gamma \frac{dv_x}{dt} = -k_r x + qE_0 - qB_0 v_z,$$

(18)

$$m_e \gamma \frac{dv_z}{dt} = qB_0 v_x.$$

(19)

Differentiating Eq. (19) with respect to time and then inputting it into Eq. (18), one can get

$$x(t) = A_1 \cos \Omega_h t + A_2 \sin \Omega_h t + A_3,$$

(20)

$$z(t) = \frac{\Omega_c}{\Omega_h}(A_1 \sin \Omega_h t - A_2 \cos \Omega_h t)$$

$$+ [v_{z0} + \Omega_c(A_3 - x_0)]t + \frac{\Omega_c}{\Omega_h}A_2 + z_0,$$

(21)

where $A_1 = x_0(1 - \Omega_c^2/\Omega_h^2) + (\Omega_c v_{z0} - qE_0/\gamma m_e)/\Omega_h^2$, $A_2 = v_{x0}/\Omega_h$, $A_3 = (\Omega_c^2 x_0 - \Omega_c v_{z0} + qE_0/\gamma m_e)/\Omega_h^2$, $\Omega_c = qB_0/\gamma m_e$, $\Omega_h = \sqrt{\Omega_c^2 + \Omega_\beta^2}$, and $\Omega_\beta = \Omega_r \equiv \sqrt{k_r/\gamma m_e}$.

B. Radiation

Using the Liénard–Wiechert potentials, the radiation spectrum of an electron on an arbitrary trajectory $\mathbf{r}(t)$ and velocity $\boldsymbol{\beta}(t) = \mathbf{v}(t)/c$ at a far field can be presented as[36]

$$\frac{d^2 I}{d\omega d\Omega} = \frac{q^2 \omega^2}{16\pi^3 c \varepsilon} \left| \int_{-\infty}^{\infty} \hat{\mathbf{n}} \times [\hat{\mathbf{n}} \times \boldsymbol{\beta}(t)] \right.$$
$$\left. \times \exp\left\{ i\omega \left[t - \frac{\hat{\mathbf{n}} \cdot \mathbf{r}(t)}{c} \right] \right\} dt \right|^2, \quad (22)$$

where I is the radiation intensity, ω is the radiation frequency, Ω is the solid angle, and $\hat{\mathbf{n}}$ is the unit vector indicating the observation point from the electron orbit. Due to the far-field approximation, $\hat{\mathbf{n}} = \mathbf{r}(t)$ and then $\hat{\mathbf{n}} \times (\hat{\mathbf{n}} \times \boldsymbol{\beta})$ becomes $-\beta_\theta \hat{\boldsymbol{\theta}} - \beta_\phi \hat{\boldsymbol{\varphi}}$. By changing β_θ and β_ϕ to the Cartesian coordinate, Eq. (22) can be rewritten as[25]

$$\frac{d^2 I_\theta}{d\omega d\Omega} = \frac{e^2 \omega^2}{16\pi^3 c \varepsilon} |\Lambda_{\beta_x} \cos\theta \cos\phi - \Lambda_{\beta_z} \sin\theta|^2, \quad (23a)$$

$$\frac{d^2 I_\phi}{d\omega d\Omega} = \frac{e^2 \omega^2}{16\pi^3 c \varepsilon} |\Lambda_{\beta_x} \sin\phi|^2, \quad (23b)$$

where

$$\Lambda_{\beta_x, \beta_z} = \int_{-T/2}^{T/2} (\beta_x, \beta_z) \exp i[\omega t - k_x x(t) - k_z z(t)] dt, \quad (24)$$

where $k_x = k \sin\theta \cos\phi$, $k_z = k \cos\theta$, and $k = \omega/c$. β_y is set to zero due to the electron's motion confined in the x-z plane. $T = N T_\beta$, with N being a positive integer. T_β is the exact betatron period determined by solving Eq. (9) and slightly differs from $2\pi/\Omega_\beta$ based on the semiclassical theory, which will be shown in Sec. III.

As will be shown later, the relativistic electron's trajectory can be expanded as

$$x(t) = \sum_{n=1}^{\infty} c_n \sin(n\omega_\beta t) + \sum_{n=0}^{\infty} c_n' \cos(n\omega_\beta t), \quad (25a)$$

$$z(t) = \bar{v}_{z0} t + \sum_{n=1}^{\infty} d_n \sin(n\omega_\beta t) + \sum_{n=0}^{\infty} d_n' \cos(n\omega_\beta t), \quad (25b)$$

where $\bar{v}_{z0} = [z(T_\beta/2) - z(-T_\beta/2)]/T_\beta$. $\omega_\beta = 2\pi/T_\beta$. The coefficients of c_n' and d_n', i.e., the cosine components, are zero in the absence of external fields (E_0 and B_0).

Using Eqs. (25a) and (25b) and the Jacobi–Anger formula,[47]

$$\exp(\pm i\xi \sin\theta) = \sum_{m=-\infty}^{\infty} J_m(\xi) \exp(\pm im\theta), \quad (26a)$$

$$\exp(\pm i\xi \cos\theta) = \sum_{m'=-\infty}^{\infty} (\pm i)^{m'} J_{m'}(\xi) \exp(\pm im'\theta), \quad (26b)$$

where $J_m(\xi)$ is the first kind Bessel function, the phase in Eq. (24) can be written as

$$\exp i[\omega t - k_x x(t) - k_z z(t)]$$
$$= \sum_{m_1^{(')}, \mu_1^{(')}=-\infty}^{\infty} \sum_{m_2^{(')}, \mu_2^{(')}=-\infty}^{\infty} \cdots \sum_{m_n^{(')}, \mu_n^{(')}=-\infty}^{\infty} \cdots \sum_{m_\infty^{(')}, \mu_\infty^{(')}=-\infty}^{\infty}$$
$$\times \Psi \exp(i\omega' t), \quad (27)$$

where the notation $m_n^{(')}, \mu_n^{(')}$ denotes the summation over m_n, m_n', μ_n, and μ_n',

$$\Psi = \prod_{n=0}^{\infty} i^{m_n' + \mu_n'} \left(\frac{-k_x c_n'}{|k_x c_n'|} \right)^{m_n'} \left(\frac{-k_z d_n'}{|k_z d_n'|} \right)^{\mu_n'}$$
$$\times J_{m_n}(|k_x c_n|) J_{m_n'}(|k_x c_n'|) J_{\mu_n}(|k_z d_n|) J_{\mu_n'}(|k_z d_n'|), \quad (28a)$$

$$\omega' = \omega - k_z \bar{v}_{z0} - \sum_{n=1}^{\infty} n \left(m_n \frac{k_x c_n}{|k_x c_n|} + \mu_n \frac{k_z d_n}{|k_z d_n|} \right) \omega_\beta$$
$$- \sum_{n=0}^{\infty} n \left(m_n' \frac{k_x c_n'}{|k_x c_n'|} + \mu_n' \frac{k_z d_n'}{|k_z d_n'|} \right) \omega_\beta. \quad (28b)$$

Due to the presence of $\bar{v}_{z0}$, the radiation frequency is no longer in units of the betatron frequency ω_β but the modified one $\omega_\beta' = \omega_\beta/(1 - \bar{v}_{z0} \cos\theta/c)$, which can be obtained by substituting $k_z = \omega \cos\theta/c$ into Eq. (28b) and then taking rearrangement. As $\bar{v}_{z0} \cos\theta/c$ approaches 1, the unit frequency ω_β' gets high.

Substituting Eq. (27) into Eq. (24) yields

$$\Lambda_{\beta_x} = N\pi \exp[-i(k_x c_0' + k_z d_0')] \sum_{m_1^{(')}, \mu_1^{(')}=-\infty}^{\infty} \sum_{m_2^{(')}, \mu_2^{(')}=-\infty}^{\infty} \cdots \sum_{m_n^{(')}, \mu_n^{(')}=-\infty}^{\infty} \cdots \sum_{m_\infty^{(')}, \mu_\infty^{(')}=-\infty}^{\infty} \Psi \sum_{\nu=1}^{\infty} \nu$$
$$\times \left\{ c_\nu \left[\sin c\left(\frac{\omega_+' T}{2\pi} \right) + \sin c\left(\frac{\omega_-' T}{2\pi} \right) \right] + i c_\nu' \left[\sin c\left(\frac{\omega_+' T}{2\pi} \right) - \sin c\left(\frac{\omega_-' T}{2\pi} \right) \right] \right\}, \quad (29a)$$

$$\Lambda_{\beta_z} = N\pi \exp[-i(k_x c_0' + k_z d_0')] \sum_{m_1^{(')},\mu_1^{(')}=-\infty}^{\infty} \sum_{m_2^{(')},\mu_2^{(')}=-\infty}^{\infty} \cdots \sum_{m_n^{(')},\mu_n^{(')}=-\infty}^{\infty} \cdots \sum_{m_\infty^{(')},\mu_\infty^{(')}=-\infty}^{\infty} \Psi$$

$$\times \left\{ \frac{\bar{v}_{z0} T_\beta}{\pi} \sin c\left(\frac{\omega' T}{2\pi}\right) + \sum_{\nu=1}^{\infty} \nu \left\{ d_\nu \left[\sin c\left(\frac{\omega_+' T}{2\pi}\right) + \sin c\left(\frac{\omega_-' T}{2\pi}\right) \right] + i d_\nu' \left[\sin c\left(\frac{\omega_+' T}{2\pi}\right) - \sin c\left(\frac{\omega_-' T}{2\pi}\right) \right] \right\} \right\}, \quad (29b)$$

where $\omega_\pm' = \omega' \pm \nu\omega_\beta$. Setting $\omega_\pm' = 0$ can then find the position of radiation peaks,

$$\omega_{peak} = \left[\sum_{n=1}^{\infty} n\left(m_n \frac{k_x c_n}{|k_x c_n|} + \mu_n \frac{k_z d_n}{|k_z d_n|} \right) \right.$$
$$\left. + \sum_{n=0}^{\infty} n\left(m_n' \frac{k_x c_n'}{|k_x c_n'|} + \mu_n' \frac{k_z d_n'}{|k_z d_n'|} \right) \pm \nu \right] \omega_\beta'. \quad (30)$$

III. RESULTS AND DISCUSSION

A. Trajectory

Unless otherwise specified, the plasma density is chosen as an experimental parameter, which is equal to 10^{18} cm^{-3}. We first consider the case without the magnetic field. Figures 2(a) and 2(b) show the transverse and longitudinal trajectories as a function of time at three different incident energies, respectively, where the initial velocity ratio $v_{x0}:v_{z0}=8:2$. Line and scatter symbols denote the relativistic and semiclassical results, respectively. The inset plots show the trajectories in the x-z plane and the velocities for the relativistic result only. As we can see, the relativistic transverse trajectory is no longer purely sinusoidal due to high-order harmonic components, in contrast to the semiclassical results. As the incident energy (E) increases, the transverse trajectory period, i.e., betatron period, of both relativistic and semiclassical results increases. The semiclassical betatron period $(2\pi/\Omega_\beta)$ is slightly larger than the relativistic one (T_β) by almost 10% increment, while the maximum value of the semiclassical transverse trajectory is about 20% lower than the relativistic one. The relativistic and semiclassical longitudinal trajectories differ much. For the relativistic case, the longitudinal velocity is closely related to the transverse velocity due to the limit of light speed, as shown in Eq. (7). When the restoring force from the ion plasma makes the transverse velocity decelerated, the longitudinal velocity accelerates and thus results in a double-peak structure in the velocity inset of Fig. 2(b), which leads to two distinct slopes in the longitudinal trajectory. The two-slope behavior explains why the Fourier expansion in Eq. (25b) needs an average initial velocity $\bar{v}_{z0}$ multiplied by time as a background. For the semiclassical case, the longitudinal trajectory only linearly depends on time.

Figures 3(a) and 3(b) show the transverse and longitudinal trajectories for three different initial velocity ratios, respectively, where the incident energy is 100 MeV. The inset plots show their velocities and trajectories in the x-z plane. As the ratio $v_{x0}:v_{z0}$ decreases, the contribution of high-order

harmonic components to trajectories decreases, and thus the relativistic effect becomes weak. The transverse trajectory reduces to be nearly sinusoidal, and the longitudinal velocity becomes weakly dependent on time. Interestingly, the transverse and longitudinal trajectories just contain odd and even harmonic components, respectively. The Fourier coefficients for the three sets of trajectories shown in Table I can prove that. The bold letter denotes important components. For the longitudinal trajectory, consider that the second harmonic components is enough when the initial velocity ratio $v_{x0}:v_{z0}$ is low, which coincides with the theory of Esarey et al.[25] However, when the ratio $v_{x0}:v_{z0}$ increases, other higher-order components are excited, and thus a fully relativistic treatment is required.

We now consider the effect of a magnetic field. Figures 4(a) and 4(b) show the transverse and longitudinal trajectories at B_0 of 200 T, respectively, where the incident energy is 10 MeV and the initial velocity ratio $v_{x0}:v_{z0}$ is 8:2. The solid and dashed lines denote the relativistic and semiclassical results, respectively. The inset plots show their velocities and trajectories in the x-z plane. The magnetic field lowers the longitudinal velocity at the former half cycle, as the inset in Fig. 4(b) shows. The longitudinal velocity of the relativistic result even lowers to be negative, while the semiclassical one keeps positive. Once the longitudinal velocity becomes negative, the cyclotron motion is born, as depicted in the orbital inset of Fig. 4(a) for the relativistic result. The critical magnetic field differs between the relativistic and the semiclassical theories. The critical magnetic field within the semiclassical theory has an analytical expression. By integrating Eq. (19) with respect to time, we can obtain $v_z - v_{z0} = \Omega_c(x-x_0)$, where setting v_z to zero yields a critical value $x_c = -v_{z0}/\Omega_c$, with x_0 being 0. If the minimum transverse trajectory x_{min} is lower than x_c, the cyclotron motion emerges, where x_{min} can be derived from Eq. (20). With some algebraic works, the critical magnetic field within the semiclassical theory can be obtained and is shown as

$$B_c = \frac{\gamma m_e \Omega_\beta}{q} \sqrt{\frac{-v_{x0}^2 + \sqrt{v_{x0}^4 + 4v_{z0}^2(v_{x0}^2 + v_{z0}^2)}}{2(v_{x0}^2 + v_{z0}^2)}}. \quad (31)$$

For the relativistic theory, integrating Eq. (3) can yield the same criterion $x_{min} < x_c$ for the cyclotron motion. However, due to the complexity of x_{min} shown in Eq. (A10b), the critical magnetic field does not have an analytic form, and thus a numerical method should be applied. Figure 5(a) shows the critical magnetic field as a function of the incident energy for the relativistic (denoted by line) and semiclassical (scatter) theories at several conditions. The critical magnetic
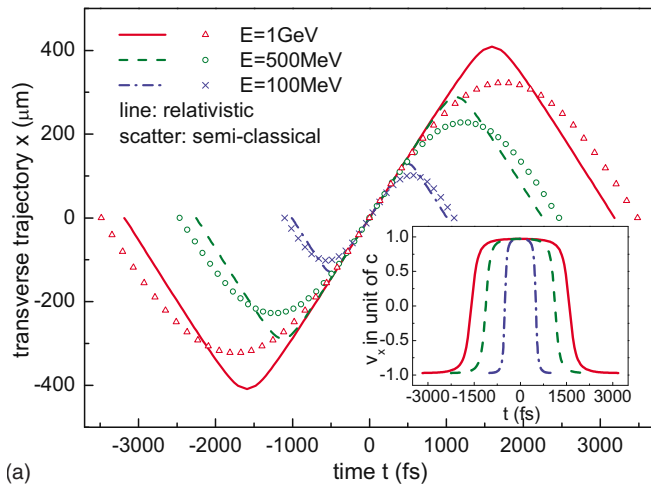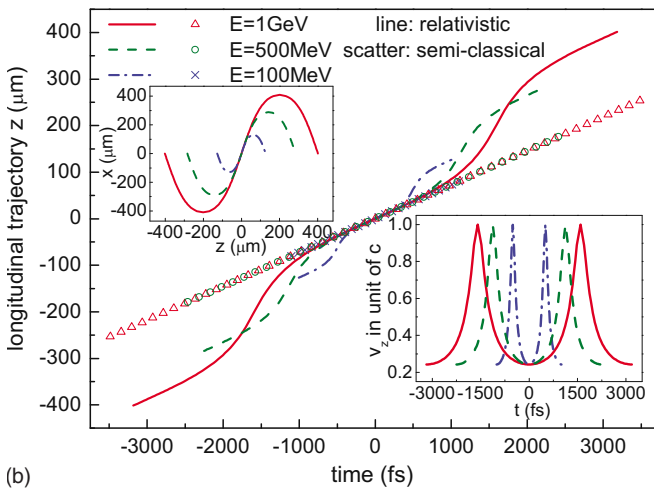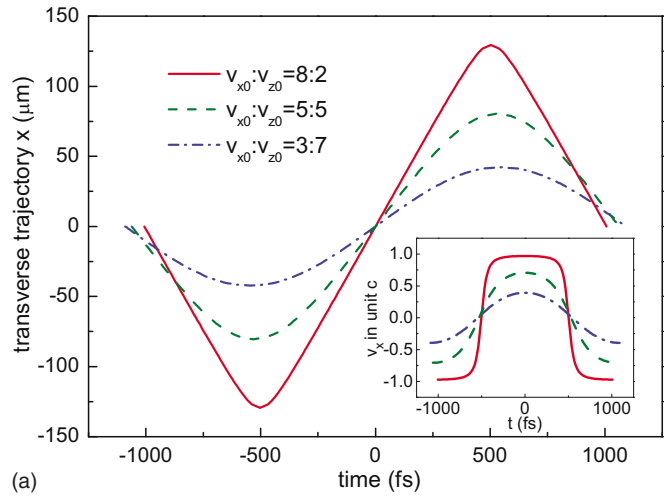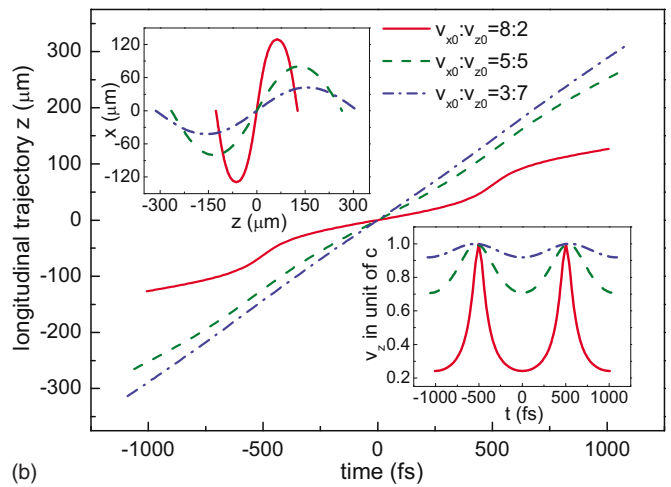
FIG. 2. (Color online) (a) Transverse trajectory and (b) longitudinal trajectory as a function of time calculated by the relativistic (abbreviated as R) and semiclassical (abbreviated as S) theories at incident energies (E) of 1 GeV (solid line for R, hollow triangle for S), 500 MeV (dashed line for R, hollow circle for S), and 100 MeV (dashed-dotted line for R, cross for S): $n_p = 10^{18}$ cm^{-3} and $v_{x0} : v_{z0} = 8 : 2$. The inset plots show the corresponding velocities and trajectories in the x-z plane for relativistic results only.

FIG. 3. (Color online) (a) Transverse trajectory and (b) longitudinal trajectory as a function of time calculated by the relativistic theory at initial velocity ratios of $v_{x0} : v_{z0} = 8 : 2$ (solid line), 5 : 5 (dashed line), and 3 : 7 (dashed-dotted line): $n_p = 10^{18}$ cm^{-3} and $E = 100$ MeV. The inset plots show the corresponding velocities and trajectory in the x-z plane.

field within the semiclassical theory is higher than that within the relativistic theory by 40% at high incident energies in the plot. As the plasma density increases, the critical magnetic field increases. The critical magnetic field at 10^{18} cm^{-3} is about three times higher than that at 10^{17} cm^{-3} for the incident energy of 10 MeV and the ratio of $v_{x0} : v_{z0} = 8 : 2$. This is because an enhanced restoring force of ion channel competes with the effect of the magnetic field, which can also be predicted by Eq. (31) even if its solution is not exact. The initial velocity ratio also influences the critical magnetic field. The critical magnetic field at $v_{x0} : v_{z0} = 5 : 5$ is closely three times higher than that at $v_{x0} : v_{z0} = 8 : 2$ for an incident energy of 20 MeV and a density of 10^{17} cm^{-3}. Since the cyclotron motion occurs as v_z decreases to zero, a stronger magnetic field is needed for a higher v_{z0} case. The critical magnetic field is an important parameter because the cyclotron motion can result in a considerable radiation spectrum and amplitude, as will be shown later.

Figure 5(b) shows the peak-to-peak amplitude of x(t) at various conditions within the relativistic (line) and semiclassical (scatter) theories, where $v_{x0} : v_{z0} = 8 : 2$. The semiclassical theory always underestimates the peak-to-peak amplitude, which decreases as the density increases. A magnetic field has a stronger effect on the peak-to-peak amplitude at 10^{17} cm^{-3} than at 10^{18} cm^{-3}. As the incident energy increases, the deviation of the peak-to-peak amplitude due to the magnetic field becomes small. Figure 5(c) shows the betatron period with the same conditions and symbolic meanings as those in Fig. 5(b). A larger betatron period in the semiclassical theory than in the relativistic theory is clearly shown. As the density increases, the betatron period decreases. In addition, a magnetic field has a stronger effect on the betatron period at 10^{17} cm^{-3} than at 10^{18} cm^{-3}, which is similar to that of the peak-to-peak amplitude.

B. Radiation

We are now going to discuss the radiation spectrum due to the betatron oscillation. First, the case without the magnetic field is considered. Figures 6(a) and 6(b) show the ra-

TABLE I. Fourier components of relativistic trajectories at various initial velocity ratios $v_{x0}:v_{z0}$. $c_n=(2/T_\beta)\int_{-T_\beta/2}^{T_\beta/2}x(t)\sin(n\omega_\beta t)dt$; $d_n=(2/T_\beta)\int_{-T_\beta/2}^{T_\beta/2}z(t)\sin(n\omega_\beta t)dt$; $E=100$ MeV; $B_0=0$; and $n_p=10^{18}$ cm^{-3}. Dominant components are denoted by bold letters.

$v_{x0}:v_{z0}$	c_1/d_1	c_2/d_2	c_3/d_3	c_4/d_4	c_5/d_5	c_6/d_6	c_7/d_7	c_8/d_8	c_9/d_9	c_{10}/d_{10}
8:2	**114.55**/ 2.94×10^{-3}	-2.03×10^{-3}/ **−12.67**	**−10.09**/ -2.56×10^{-3}	3.87×10^{-3}/ **3.19**	**2.69**/ 1.81×10^{-3}	-5.36×10^{-3}/ **−1.17**	**−0.96**/ -1.13×10^{-3}	6.51×10^{-3}/ **0.50**	0.39/ 6.07×10^{-4}	-7.39×10^{-3}/ -0.23
5:5	**77.84**/ -4.63×10^{-4}	5.79×10^{-4}/ **−7.24**	**−2.30**/ 2.12×10^{-4}	-7.11×10^{-4}/ **0.53**	0.15/ 1.02×10^{-4}	2.95×10^{-4}/ -5.35×10^{-2}	2.4×10^{-2}/ -1.26×10^{-4}	8.10×10^{-5}/ 2.39×10^{-3}	-3.34×10^{-2}/ -1.70×10^{-4}	2.14×10^{-4}/ 3.67×10^{-3}
3:7	**41.93**/ 5.53×10^{-5}	-5.40×10^{-4}/ **−2.10**	-0.29/ -1.18×10^{-4}	1.32×10^{-3}/ 3.73×10^{-2}	-2.46×10^{-2}/ 7.26×10^{-5}	-1.82×10^{-3}/ 2.57×10^{-4}	2.51×10^{-2}/ 3.59×10^{-7}	1.89×10^{-3}/ -1.20×10^{-3}	-1.92×10^{-2}/ 6.80×10^{-6}	-1.93×10^{-3}/ 1.21×10^{-3}

diation spectrum within the semiclassical theory and the theory of Esarey *et al.*, respectively, where the electron's incident energy is 100 MeV, the density is 10^{18} cm^{-3}, the betatron oscillation number N=10, $\theta=0°$, and $\phi=0°$. The polar angle ϕ is set to zero for all results. From Eq. (23b), we know that no radiation along the polar direction I_ϕ exists. Hence, only radiation along the azimuth direction I_θ in this report was considered. At $\theta=0°$, Eq. (24) tells us that only longitudinal trajectory contributes to radiation spectrum. Since the result of Esarey *et al.* has the second harmonic component in z(t), its spectrum is broader than that of the semiclassical result and shows an odd-order radiation. The unit frequency ω'_β of Fig. 6(b) is larger than that of Fig. 6(a) because the average initial longitudinal velocity $\bar{v}_{z0}$ in Eq. (25b) has been taken into the result of Esarey *et al.* as well as a larger period in the semiclassical theory than in the relativistic theory. Due to the velocity enhancement, as shown in Fig. 2(b), $\bar{v}_{z0}$ is faster than v_{z0} and makes ω'_β higher, where $\omega'_\beta=\omega_\beta/(1-\bar{v}_{z0}\cos\theta/c)$ is derived from Eq. (28b). In Fig. 6(b), both Jacobi–Anger expansion (denoted by line) and Gaussian quadrature method (scatter) are applied to calculate the radiation spectrum, where they show a good agreement due to sufficient mode number for the Jacobi–Anger expansion in Eq. (26a), with the error between the left- and right-hand sides of Eq. (26a) being lower than 0.1%.

Figures 7(a) and 7(b) show the radiation spectrum within the relativistic theory by using Jacobi–Anger expansion and Gaussian quadrature methods, respectively, where the conditions are the same as those in Figs. 6(a) and 6(b). For the method of Jacobi–Anger expansion, three dominant components, i.e., the second, fourth, and sixth order harmonics, shown in Table I were considered. The mode number for Bessel function was chosen such that the error is lower than 0.1%. For Gaussian quadrature method, 96 quadrature points per $250\omega'_\beta$ was applied, that is, 96 points for $\omega\leq250\omega'_\beta$, 192 points for $250\omega'_\beta<\omega\leq500\omega'_\beta$, and so on were taken. The radiation spectrum from the Gaussian quadrature method is more accurate than that from the Jacobi–Anger method because Eq. (24) is integrated without any expansion. By comparing Figs. 7(a) and 7(b), we found that the spectrum of the Gaussian quadrature method is ten times that of the Jacobi–Anger expansion. This demonstrates that minor harmonic components (d_8, d_{10}, etc.) still have a considerable contribution to the radiation, which thus should not be neglected. The significant difference between Figs. 7(a) and 7(b) is not due to insufficient Bessel functions in Eq. (26a) since the accuracy with error less than 0.1% shows a good agreement with

the result of Esarey *et al.* in Fig. 6(b) between the two methods. Comparing Figs. 6(b) and 7(b), one can find that the trajectory of Esarey *et al.* is unable to describe the realistic radiation spectrum at the high initial velocity ratio of $v_{x0}:v_{z0}=8:2$. A two-order difference in the spectrum width and a one-order difference in amplitude are shown.

The radiation spectrum starts from ω'_β due to Eq. (30), with ν being 1 and other two summations being zero. The spacing between radiation peak and peak is determined by the trajectory z(t). Since z(t) is consisted of even harmonic components, Eq. (30) tells us that the radiation peak has $2\omega'_\beta$ spacing for even n. Consequently, the on-axis radiation ($\theta=0°$) shows only odd-order peaks. Although the Jacobi–Anger expansion is good to explain radiation result analytically, its calculation is much more time-consuming than that of the Gaussian quadrature method. For example, when only six harmonic components (c_1,c_3,c_5,d_2,d_4,d_6) are taken into Eq. (24) for an off-axis case ($\theta\neq0$) at $\omega\sim1000\omega'_\beta$, the calculating time already increases to the day scale, where the code was written in C++ ran in computer with dual-Xeon CPU at 2.66 GHz and 32 Gbyte RAM (random access memory). Hence, the Gaussian quadrature method is used for the following results.

Figures 8(a) and 8(b) show the radiation spectrum at $\theta=30°$ within the relativistic and theories of Esarey *et al.*, respectively, where other conditions are the same as above. The inset plot of Fig. 8(b) shows the semiclassical result. The large difference between the results of Esarey *et al.* and the relativistic results confirms that the trajectory of Esarey *et al.* cannot describe the radiation spectrum at a high initial velocity ratio $v_{x0}:v_{z0}$. For an off-axis case, the transverse trajectory can contribute to radiation according to Eq. (24). Since x(t) is consisted of odd modes shown in Table I, the radiation peak becomes ω'_β spacing by Eq. (30), where n $=1$ and $m_1=1$, in contrast to the on-axis one with $2\omega'_\beta$ spacing. Thus, both odd and even order peaks exist in the radiation spectrum. The unit frequency ω'_β is slightly lower than the on-axis one due to a decreased cosine value in $\omega'_\beta=\omega_\beta/(1-\bar{v}_{z0}\cos\theta/c)$. Even so, the spectrum width at $\theta=30°$ is still almost four times broader than that at $\theta=0°$, while the radiation amplitude at $\theta=30°$ is twice higher than the on-axis one. The angular dependence is quite different from that at a low initial velocity ratio, whose radiation is strongest on the axis shown below. As θ increases, the spectrum width and the radiation amplitude continue to increase. At $\theta=60°$, the spectrum width can even spread to
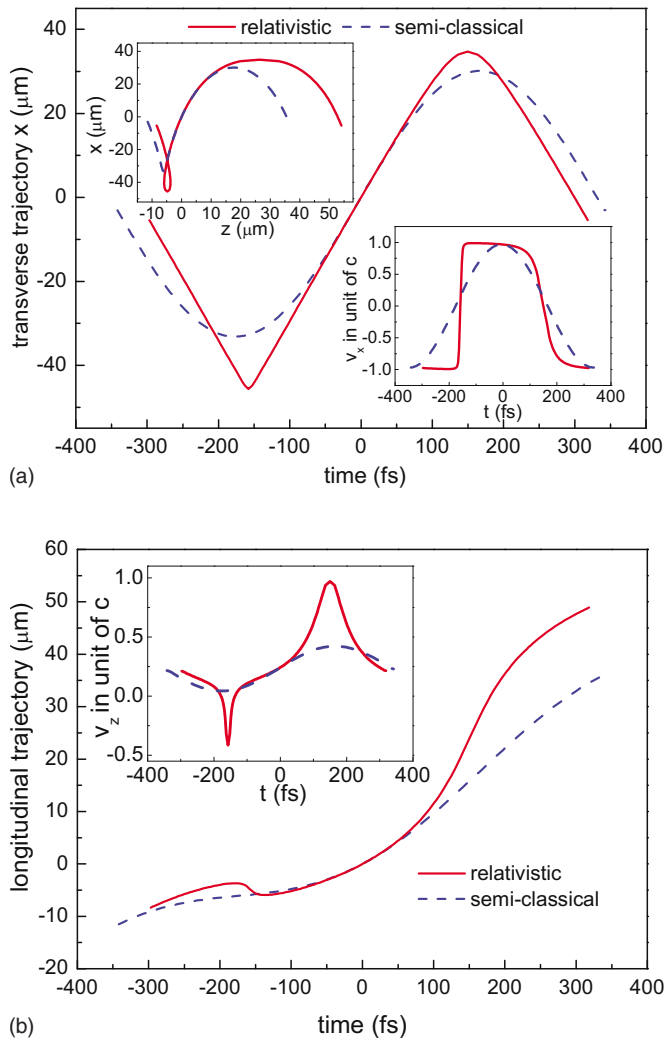
FIG. 4. (Color online) (a) Transverse trajectory and (b) longitudinal trajectory as a function of time in the presence of magnetic field $B_0=200$ T calculated by the relativistic (solid line) and semiclassical (dashed line) theories: $n_p=10^{18}$ cm^{-3} and E=10 MeV. The inset plots show the corresponding velocities and trajectories in the x-z plane.

$1.2\times10^6\omega'_\beta$ ($\omega'_\beta=4.0$ THz), as shown in Fig. 9(a), and the radiation amplitude rises to a value that is about 150 times higher than the on-axis one. The feature of broad and large radiation spectrum is more obvious when a strong enough magnetic field is applied. After θ exceeds a critical value, the spectrum width and radiation amplitude begin to decrease. At $\theta=90°$, the spectrum width and radiation amplitude, as shown in Fig. 9(b), reduce to about $140\omega'_\beta$ and 10^{-17} Ws/m^2, respectively, which become lower than those of the on-axis radiation.

Figure 10(a) shows the on-axis radiation spectrum at a low initial velocity ratio $v_{x0}:v_{z0}$ as 2:8 from the relativistic trajectory and from the trajectory of Esarey *et al.*, respectively, where other conditions are the same as those described before. Solid-square and hollow-triangular symbols denote the relativistic result and that of Esarey *et al.*, respectively. The inset plots show the semiclassical results. As we can see, at a low initial velocity ratio, the trajectory of Esarey *et al.* is well to predict both the width and the amplitude of radiation spectrum because very few high-order harmonic
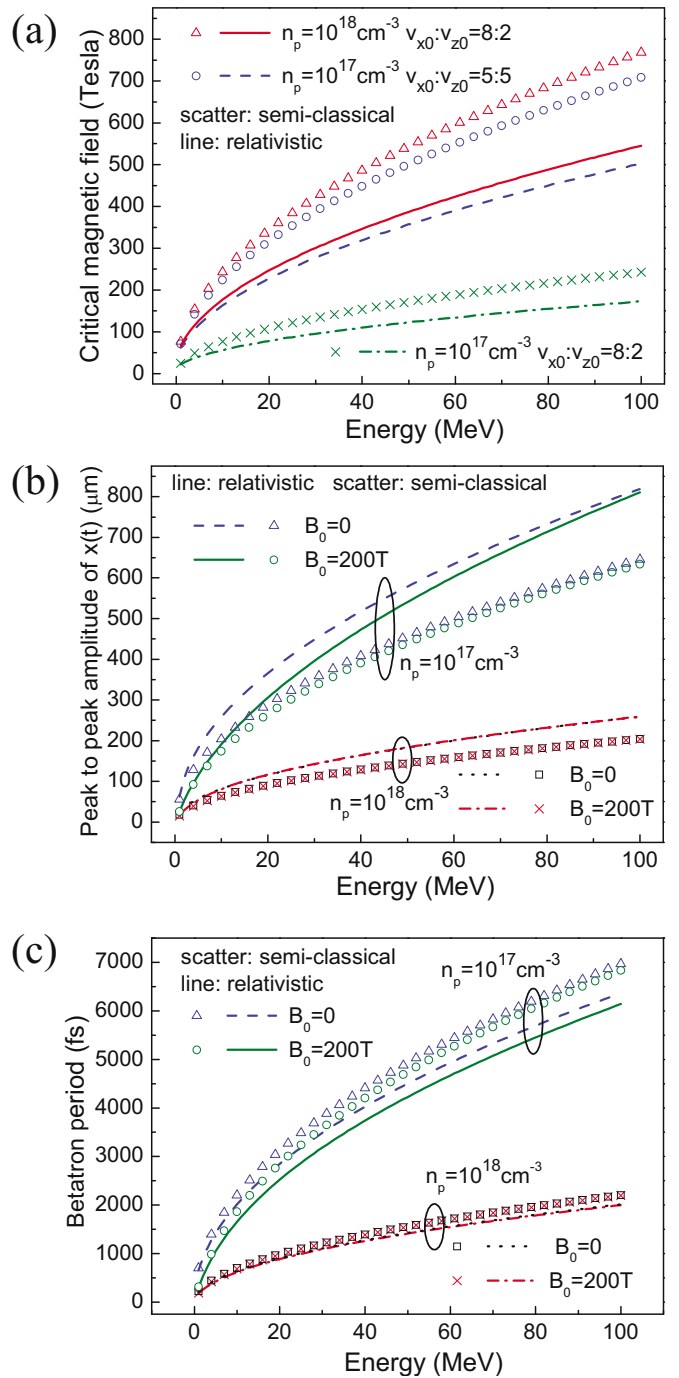

FIG. 5. (Color online) (a) Critical magnetic field for cyclotron motion as a function of the incident energy calculated by the relativistic (R) and semiclassical (S) theories at three sets of conditions: (i) $n_p=10^{18}$ cm^{-3}, $v_{x0}:v_{z0}$ =8:2 (solid line for R, hollow triangle for S); (ii) $n_p=10^{17}$ cm^{-3}, $v_{x0}:v_{z0}$ =5:5 (dashed line for R, hollow circle for S); and (iii) $n_p=10^{17}$ cm^{-3}, $v_{x0}:v_{z0}=8:2$ (dashed-dotted line for R, cross for S). (b) Peak-to-peak amplitude of x(t) and (c) oscillation period as a function of energy at $v_{x0}:v_{z0}$ =8:2 with four sets of conditions: (i) $n_p=10^{17}$ cm^{-3}, $B_0=200$ T (solid line for R, hollow circle for S); (ii) $n_p=10^{17}$ cm^{-3}, $B_0=0$ (dashed line for R, hollow triangle for S); (iii) $n_p=10^{18}$ cm^{-3}, $B_0=200$ T (dashed-dotted line for R, cross for S); and (iv) $n_p=10^{18}$ cm^{-3}, $B_0=0$ (dotted line for R, hollow square for S).
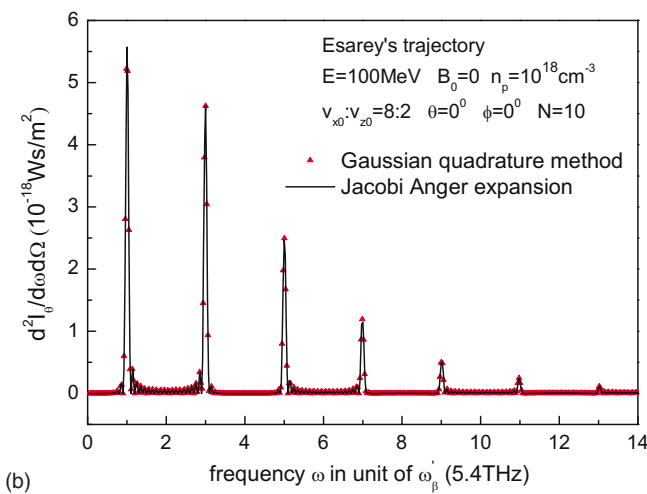
components are involved in the trajectories, as shown in Table I. The second harmonic component in z(t) is important. Without it, the result becomes semiclassical and fails to describe the radiation spectrum. Due to the high initial longi-
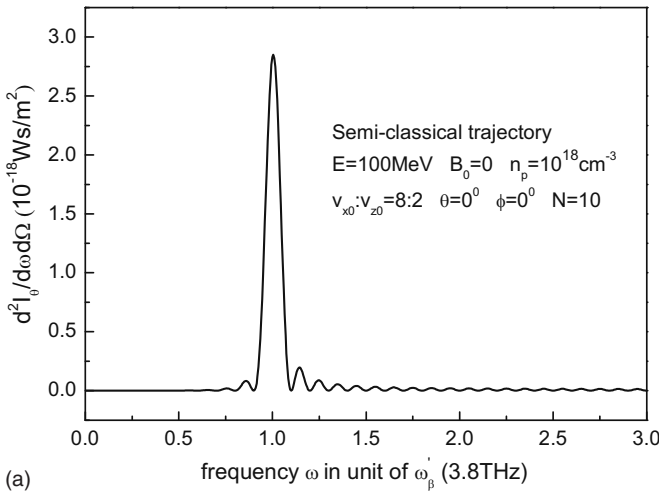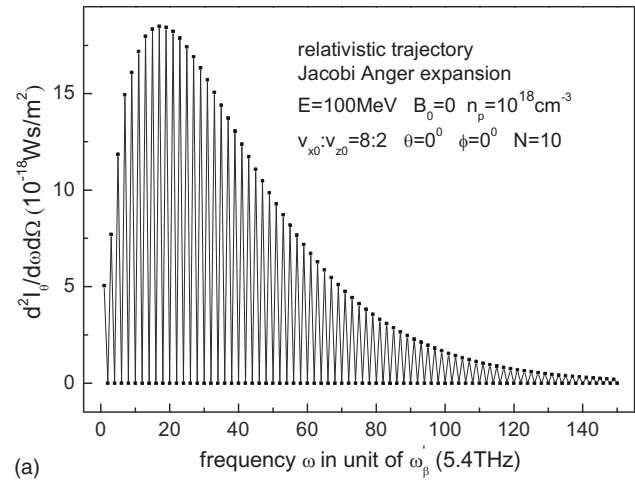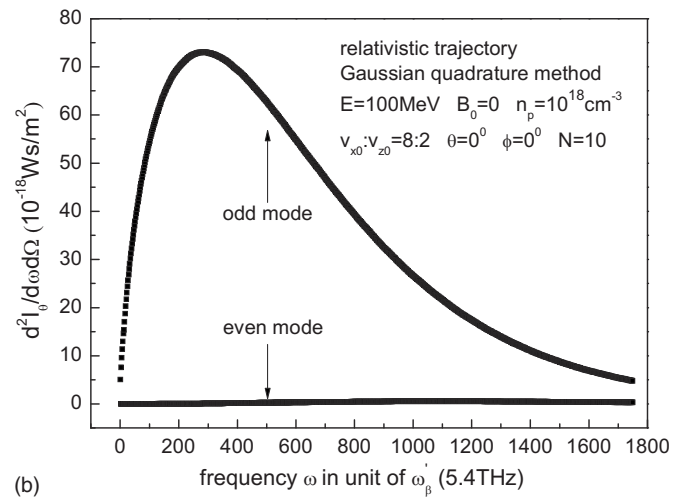
FIG. 6. (Color online) (a) Radiation intensity spectrum of the semiclassical trajectory at E=100 MeV, $B_0=0$, $n_p=10^{18}$ cm^{-3}, $v_{x0}:v_{z0}=8:2$, azimuth angle $\theta=0°$, polar angle $\phi=0°$, and oscillation number N=10. (b) Radiation spectrum of the trajectory of Esarey *et al.* [z(t) with the second harmonic term] using the Gaussian quadrature method (triangle) and Jacobi–Anger expansion (solid line) with the same conditions as those in Fig. 6(a).

FIG. 7. Radiation intensity spectrum of the relativistic trajectory using (a) the Jacobi–Anger expansion and (b) the Gaussian quadrature method with the same conditions as those in Fig. 6(a).

tudinal velocity, the unit frequency ω'_β is high and can be as large as 189.1 THz, which is almost twice higher than the semiclassical one. As θ increases, the spectrum width and the radiation amplitude decrease monotonously, as shown in Fig. 10(b) for $\theta=30°$ and Fig. 10(c) for $\theta=60°$, unlike the case at a high initial velocity ratio. The result of Esarey *et al.* (denoted by scatter) shows a good agreement with the relativistic one (line). In addition, as θ increases, the radiation becomes dominated by x(t) rather than by z(t) due to an increasing k_x and a decreasing k_z, as shown in Eq. (24). Since x(t) is mostly consisted of the lowest harmonic component for the low initial velocity ratio in Table I, the radiation spectrum at a high enough θ, such as the case of $\theta=60°$, can be even described by the semiclassical result, as shown in the inset of Fig. 10(c).

We now present the results with a magnetic field. Figures 11(a) and 11(b) show the on-axis radiation spectrum at densities of 10^{17} and 10^{18} cm^{-3}, respectively, where $B_0=60$ T (denoted by solid scatter), the incident energy is

10 MeV, $v_{x0}:v_{z0}=8:2$, and N=3. The magnetic field can create a cyclotron motion for the density at 10^{17} cm^{-3} but cannot for 10^{18} cm^{-3}. The incident energy is chosen to be low to keep the magnetic field experimentally achievable. If the incident energy is 100 MeV, the critical magnetic field increases to hundreds of tesla, according to Fig. 5(a). The result without the magnetic field is also shown for comparison and denoted by hollow scatter. First, as we can see, the magnetic field moves the radiation spectrum to a higher-frequency region considerably for 10^{17} cm^{-3}, while a little for 10^{18} cm^{-3}. In Fig. 11(a), the spectrum with B_0 field shows roughness below $100\omega'_\beta$, which is actually an oscillation, as shown in the right-side inset. ω'_β is larger at 10^{18} cm^{-3} than at 10^{17} cm^{-3} due to a stronger restoring force from the ion channels. The inset plots also show the semiclassical results, which fail to describe the radiation spectrum. Second, the on-axis radiation shows even modes because z(t) with a magnetic field begins to contain odd harmonic terms and can make even $n\mu_n(k_z d_n/|k_z d_n|) + n\mu'_n(k_z d'_n/|k_z d'_n|) \pm \nu$ in Eq. (30), where $k_x=0$ for $\theta=0°$ and ν is odd. At 10^{17} cm^{-3}, even modes are already comparable to odd modes, while at 10^{18} cm^{-3}, even modes are still lower
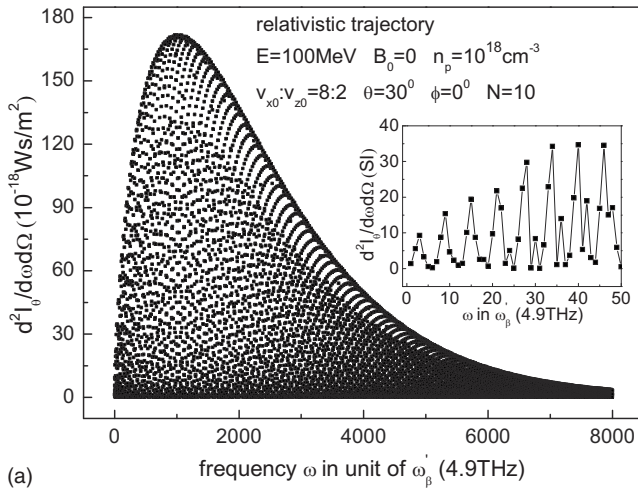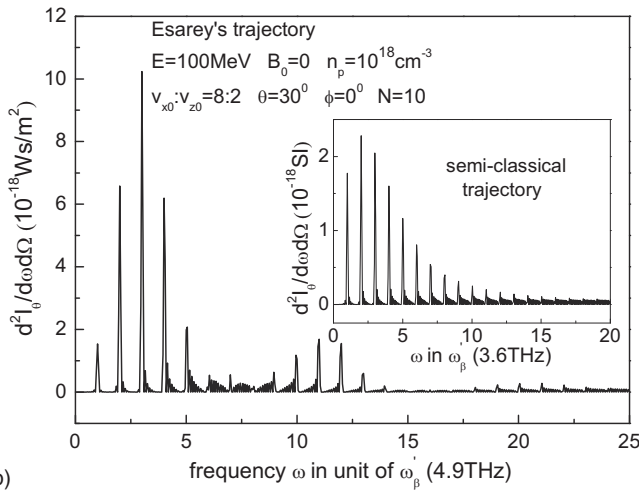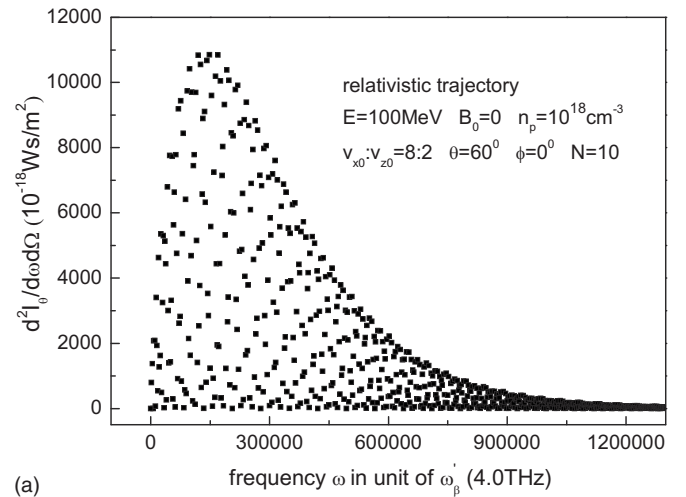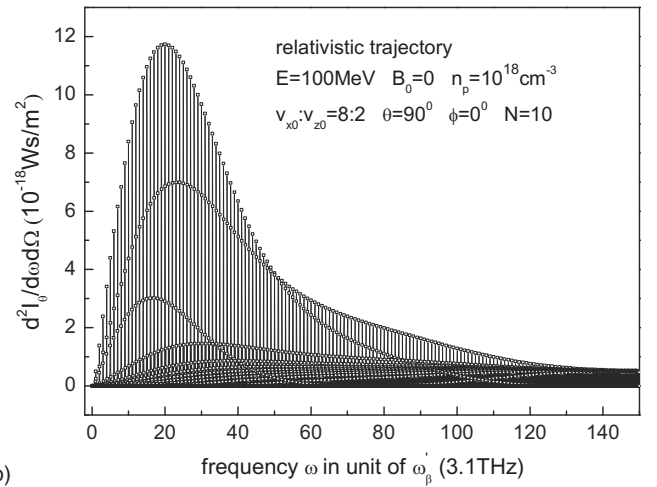
FIG. 8. Radiation intensity spectrum of (a) the relativistic trajectory and (b) the trajectory of Esarey *et al.* at $\theta=30°$. Other conditions are the same as those in Fig. 6(a). The inset of (a) shows the enlarged diagram. The inset of (b) shows the semiclassical result.

FIG. 9. Radiation intensity spectrum of the relativistic trajectory (a) at $\theta=60°$ and (b) at $\theta=90°$. Other conditions are the same as those in Fig. 6(a).

than odd modes. With the two points, we can see that a cyclotron motion results in a clear difference between the radiation spectra.

Experimentally, to generate a magnetic field as high as 60 T is still a challenge. For superconductor magnets, today's limit[48,49] is only about 25 T due to constraints of critical field, temperature, and current density. In contrast, resistive magnets are not constrained by any physical effects, which need electric power and efficient cooling. Thus, in principle, it is possible to generate any high magnetic field. However, due to the question of economics, today's limit for resistive magnets[50] can only reach 45 T, while the required power already exceeds 40 MW. A cost-effective means is hybrid magnets, a combination of superconducting and resistive magnets, which can provide magnetic fields[50] between 30 and 45 T, and a maximum of 60 T within the infrastructure.[51] All magnitudes mentioned above refer to continuous magnetic fields. If the constraint of continuous operation is removed, a higher magnetic field can be obtained, while the required power can be further reduced. Such pulse magnetic fields can be generated by capacitor driven magnet[52] or con-

trolled waveform magnets,[50] which differ from the spontaneous short-pulsed magnetic fields driven by laser-plasma interactions.[39–43] Nowadays, a magnetic field of 80 T with 7 ms is available.[53] The pulse duration is 10^8 times longer than betatron oscillation time of 70 ps estimated by Fig. 5(c) with N=10. As the pulse width of magnetic fields decreases, the required power and cost for pulse magnets decrease. Thus, the means may be applied to our experiment more feasibly.

Next, we consider the angular dependence. Figures 12(a) and 12(b) show the radiation spectrum with B_0 at densities of 10^{17} and 10^{18} cm^{-3}, respectively, where $\theta=30°$ and other parameters were kept the same as above. The solid line and scatter symbol denote the results with distinct integration accuracies, where $30(60)/250\omega'_\beta$ is taken for Fig. 12(a) and $240(480)/250\omega'_\beta$ for Fig. 12(b). $N_d/250\omega'_\beta$ (N_d = 30, 60, 240, 480) presents n × N_d × 96 Gaussian quadrature points within $250(n-1)\omega'_\beta \le \omega \le 250n\omega'_\beta$, with n being a positive integer. For 10^{17} cm^{-3}, the radiation spectrum is extremely broad. Note that the horizontal axis has been changed to the unit of $1000\omega'_\beta$ as well as that in Fig. 12(b). The spectrum only below $10^7\omega'_\beta$ (186 keV) is shown due to the limit of calculation time (more than 2 days). However,
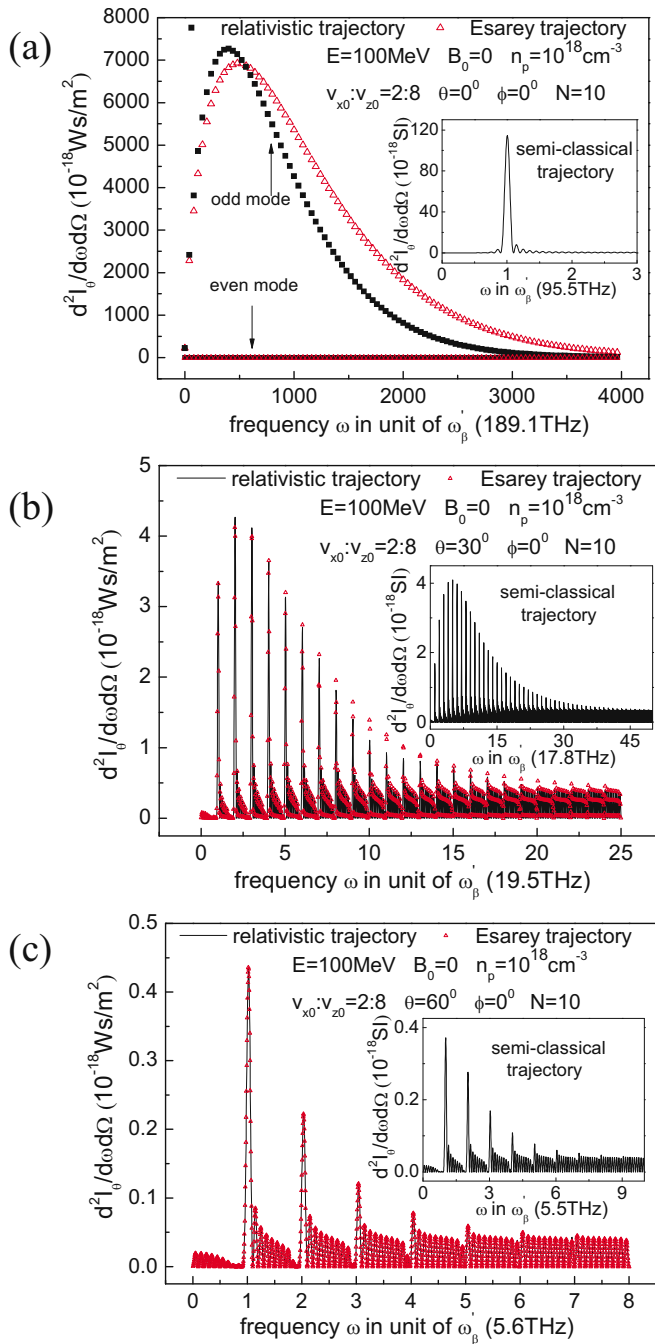
FIG. 10. (Color online) Radiation intensity spectrum for the low initial velocity ratio $v_{x0}:v_{z0}=2:8$ of the relativistic trajectory (denoted by solid line) and the trajectory of Esarey *et al.* (hollow triangle) at (a) $\theta=0°$, (b) $\theta=30°$, and (c) $\theta=60°$. Other conditions are the same as those in Fig. 6(a). The inset plots show the radiation spectra of semiclassical trajectory.
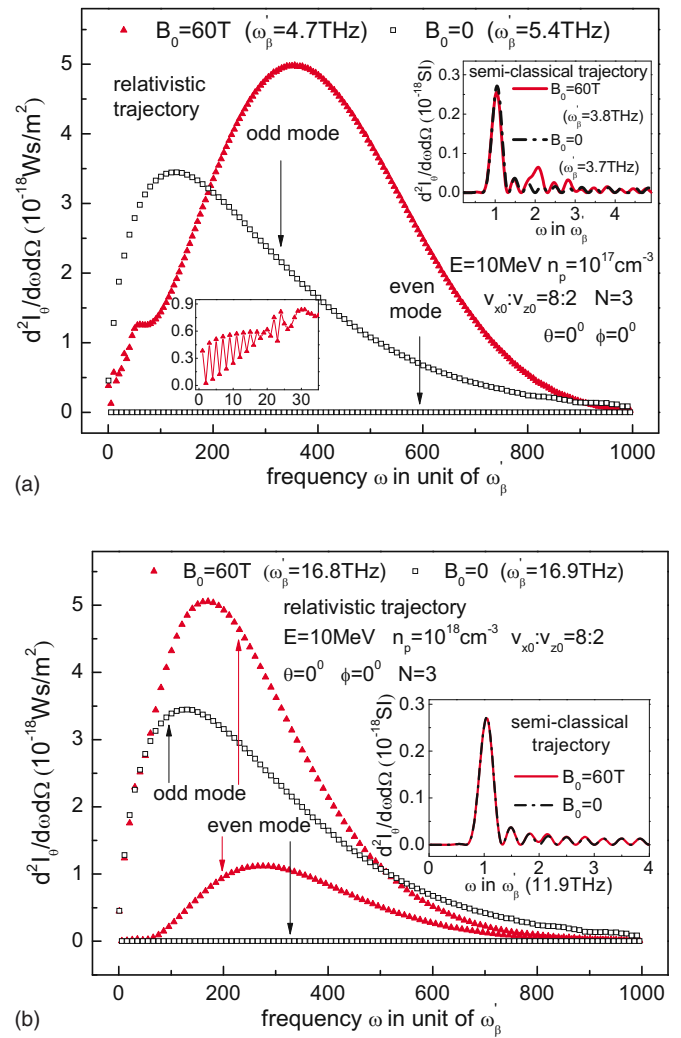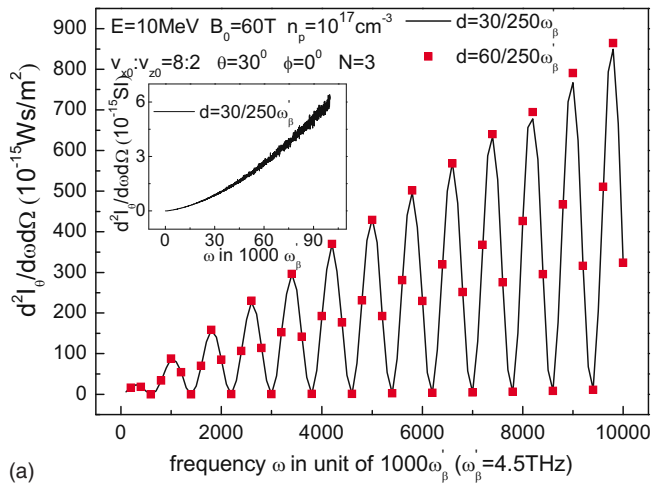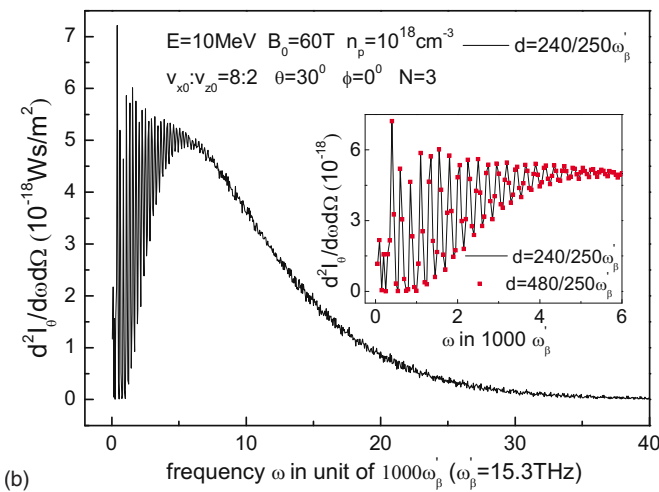

FIG. 11. (Color online) Effect of the magnetic field on the radiation intensity spectrum of the relativistic trajectory at (a) $n_p=10^{17}$ cm^{-3} and (b) $n_p=10^{18}$ cm^{-3}. The spectra with and without the magnetic field ($B_0=60$ T) are denoted by solid triangle and hollow square, respectively; $E=10$ MeV, $v_{x0}:v_{z0}=8:2$, $\theta=0°$, $\phi=0°$, and $N=3$. The inset plots show the results of semiclassical trajectory (with B_0: solid line; without B_0: dashed-dotted line) and the enlarged diagram.

the value is already 10 000 times broader than the on-axis spectrum width and exceeds the upper limit of hard x ray (120 keV). Furthermore, the spectrum may be only a fraction of the whole spectrum when compared to Fig. 8(a) and the inset of Fig. 8(a), where horizontal scales differ by 160 times. Meanwhile, the radiation amplitude is remarkably large, where the vertical axis is in units of 10^{-15} W/m^2, and the maximum amplitude is even 1.6×10^5 times stronger than the on-axis one. In contrast, for 10^{18} cm^{-3}, the spectrum is significantly (>100 times) narrower and (>1.6×10^5

times) weaker than that for 10^{17} cm^{-3}. This doubly confirms the effect of the cyclotron motion on the radiation spectrum. Otherwise, the spectrum for 10^{18} cm^{-3} at $\theta=30°$ is (~34 times) broader than that at $\theta=0°$ due to high initial velocity ratio $v_{x0}:v_{z0}$, where x(t) contains many harmonic terms and becomes important for radiation as θ increases [Eq. (24)]. The data below $5\times10^3\omega'_\beta$ in Fig. 12(b) seem rough, which actually are oscillations as shown in the inset, which the agreement between results with two integration accuracies proves it. The oscillation also appears at large scales, as shown in Fig. 12(a).

Figures 13(a) and 13(b) show the radiation spectrum with B_0 for densities of 10^{17} and 10^{18} cm^{-3}, respectively, where $\theta=45°$ and other parameters were kept the same. The solid line and scatter symbol denote the results with distinct integration accuracies, which confirm the numerical accuracy. The data seem rough because only a fraction of spectrum is shown, which is similar to the inset in Fig. 8(a). If the
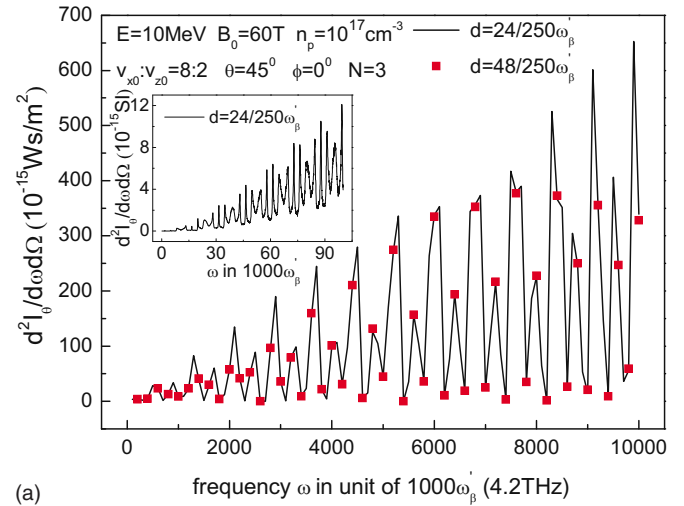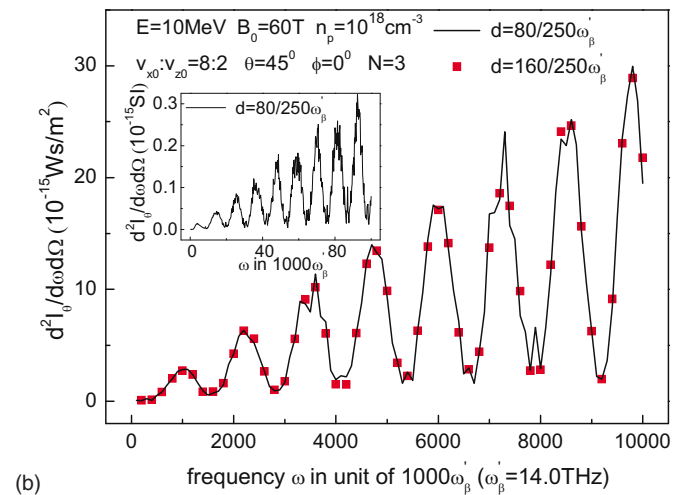
FIG. 12. (Color online) Radiation intensity spectrum (solid line) with B_0 (60 T) of the relativistic trajectory at $\theta = 30°$ for (a) $n_p = 10^{17}$ cm^{-3} and (b) $n_p = 10^{18}$ cm^{-3}. Other conditions are the same as those in Fig. 11(a). The inset plots show the enlarged diagrams. The results calculated using the twice integration accuracy better than that of solid line are denoted by solid square. A good agreement between them is demonstrated.

FIG. 13. (Color online) Radiation intensity spectrum (solid line) with B_0 (60 T) of the relativistic trajectory at $\theta = 45°$ for (a) $n_p = 10^{17}$ cm^{-3} and (b) $n_p = 10^{18}$ cm^{-3}. Other conditions are the same as those in Fig. 11(a). The inset plots show the enlarged diagrams. The results calculated using the twice integration accuracy better than that of solid line are denoted by solid square. A good agreement between them is demonstrated.

whole spectrum is shown, the result will look like that in Fig. 8(a). For 10^{17} cm^{-3}, the spectrum variation is more rapidly than that at $\theta = 30°$, as well as the fine diagram shown in the inset. Meanwhile, the radiation amplitude does not differ much from that at $\theta = 30°$. In contrast, for 10^{18} cm^{-3}, the radiation amplitude increases considerably when θ varies from $30°$ to $45°$. Note that the vertical axis of Fig. 13(b) is in units of 10^{-15} W/m^2. The maximum amplitude is about 6000 times larger than that at $\theta = 0°$ (or $\theta = 30°$). In addition, the spectrum also broadens significantly, which is at least 8000 times wider than at $\theta = 0°$ and 300 times wider than that at $\theta = 30°$. In the inset of Fig. 13(b), the roughness is actually an oscillation, as that shown in the inset of Fig. 12(b). As θ further increases to $90°$, the radiation for 10^{17} cm^{-3} shown in Fig. 14(a) still keeps a very broad spectrum and very high amplitude, while the radiation for 10^{18} cm^{-3} shown in Fig. 14(b) quickly shrinks to $\sim 2000 \omega_\beta'$ spectrum and reduces its amplitude at 10^{-18} W s/m^2. This demonstrates again the effect of the cyclotron motion on radiation.

Finally, we consider the radiation with B_0 at a low initial velocity ratio. Figures 15(a)–15(c) show the radiation spectrum at $\theta = 0°, 30°, 60°$, respectively, where $v_{x0} : v_{z0} = 2:8$, the density is 10^{17} cm^{-3}, and other parameters were kept the same as above. As θ increases, the spectrum width shrinks monotonously, and the radiation amplitude reduces quickly. The radiation spectrum is broadest and strongest at $\theta = 0°$. The maximum spectrum width is about $700\omega_\beta'$ ($\omega_\beta' = 110.3$ THz). The value is at least 500 times narrower than that for the high initial velocity ratio at the same density and $\theta = 30°$ [Fig. 12(a)], where the spectrum width is temporally assumed as $10^7 \omega_\beta'$. Furthermore, the radiation amplitude at the low initial velocity ratio is significantly weaker than that at the high initial velocity ratio. The difference between the amplitudes of two initial velocity ratios is at least 9000 times, as estimated in Figs. 12(a) and 15(a). The initial velocity ratio leading to a great difference for the radiation spectrum with B_0 is thus demonstrated. The inset
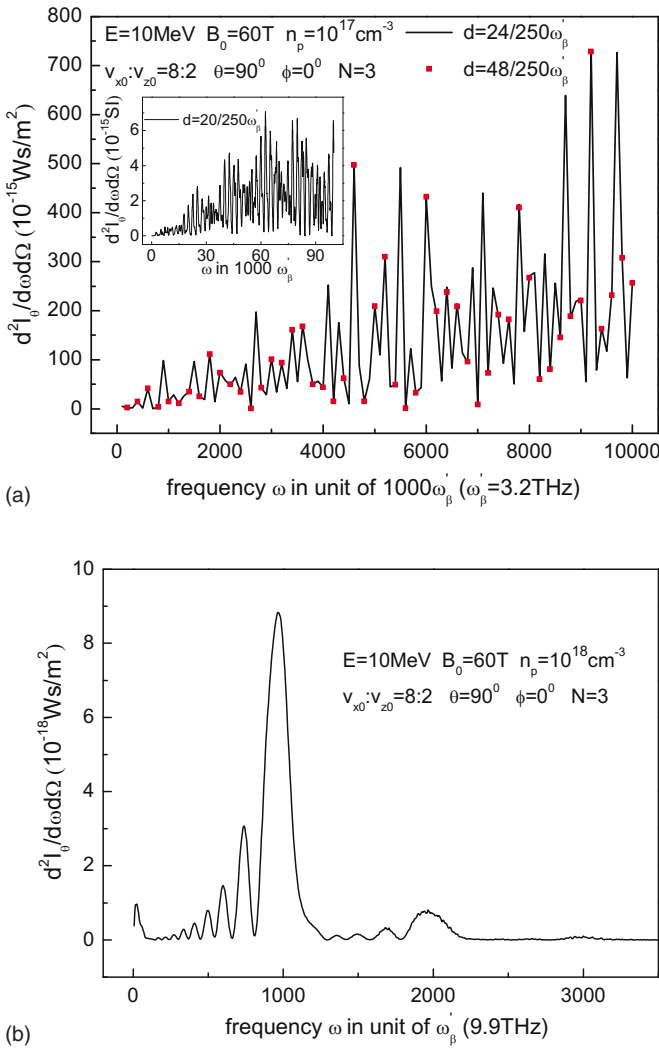
FIG. 14. (Color online) Radiation intensity spectrum (solid line) with B_0 (60 T) of the relativistic trajectory at $\theta=90°$ for (a) $n_p=10^{17}$ cm^{-3} and (b) $n_p=10^{18}$ cm^{-3}. Other conditions are the same as those in Fig. 11(a). The inset plots show the enlarged diagrams. The results calculated using the twice integration accuracy better than that of solid line are denoted by solid square. A good agreement between them is demonstrated.

FIG. 15. Radiation intensity spectrum of the relativistic trajectory for low initial velocity ratio $v_{x0}:v_{z0}=2:8$ at (a) $\theta=0°$, (b) $\theta=30°$, and (c) $\theta=60°$. Other conditions are the same as those in Fig. 11(a). The inset plots show the results of semiclassical trajectory.

plots show semiclassical results, which fail to describe radiation spectrum even at a large θ, unlike the case without B_0, as shown in Fig. 10(c).

IV. CONCLUSION

In conclusion, we analytically solve the relativistic equation of motion for betatron oscillation in ion plasma channels and numerically show trajectories as well as radiation spectra. The relativistic effect on the trajectory of betatron oscillation is strong when the initial velocity ratio ($v_{x0}:v_{z0}$) of incident electrons is high. Many high-order harmonic terms are excited in both transverse and longitudinal trajectories, which result in a quite broad and intense radiation spectrum emitting along the off axis. Otherwise, when the initial velocity ratio is low, the relativistic effect becomes weak. Only the first and second harmonic terms remain in the transverse and longitudinal trajectories, respectively, as described by Esarey et al.[25] The strongest radiation emits along the axis
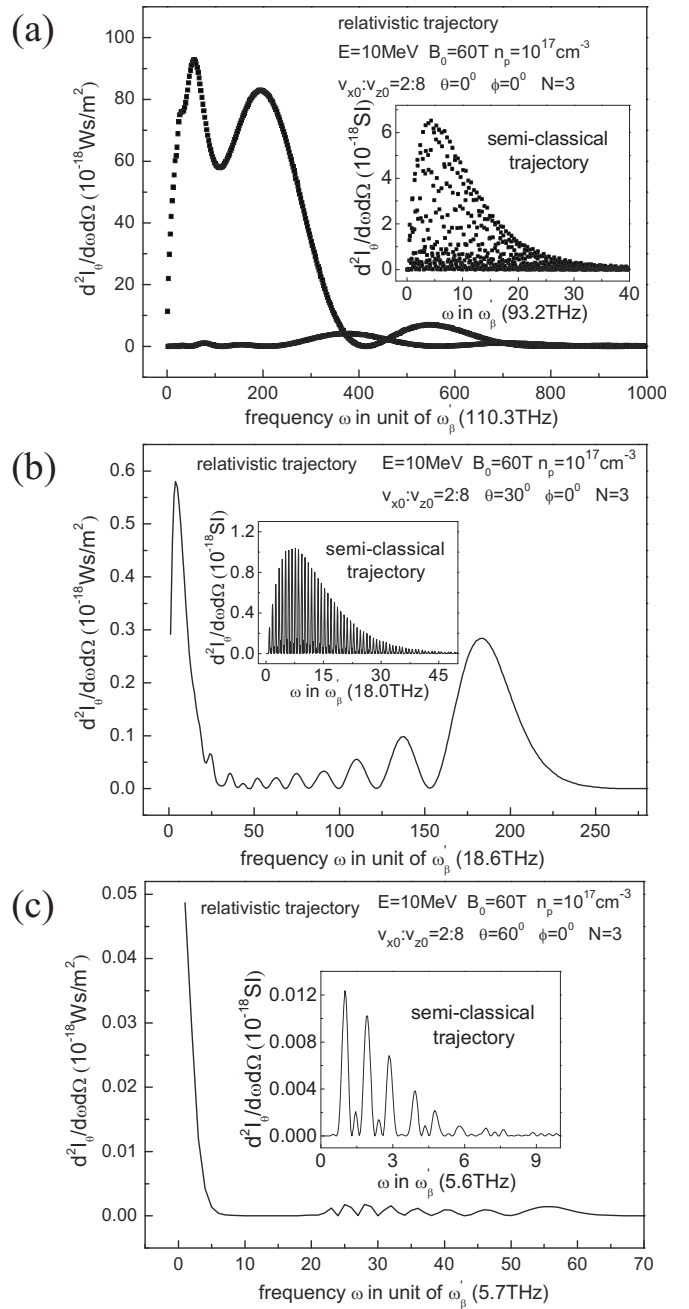
($\theta=0$), whose spectrum and amplitude are narrower and weaker than those at a high initial velocity ratio, respectively. Such spectrum difference between high and low initial velocity ratios ($v_{x0}:v_{z0}$) is significantly multiplied when a cyclotron motion occurs due to more fruitful harmonic terms. With a cyclotron motion, the radiation spectrum for a high initial velocity ratio ($v_{x0}:v_{z0}$) is immensely broad and extremely strong, which can enter into the gamma-ray region with a wide angular distribution of radiation. A new method to emit γ ray is demonstrated.

APPENDIX: SOLUTIONS OF THE QUARTIC EQUATION (REF. 54)

Equation (11) can be simply written as

$$x^4 + a_1 x^3 + a_2 x^2 + a_3 x + a_4 = 0, \tag{A1}$$

where $a_1 = -4\omega_r^{-2}\widetilde{E}_0$, $a_2 = 4\omega_r^{-4}(\widetilde{E}_0 - \gamma_0\omega_r^2 - \omega_c^2)$, $a_3 = 8\gamma_0\omega_r^{-4}(\widetilde{E}_0 - \omega_c v_{z0}/c)$, and $a_4 = 4\omega_r^{-4}[\gamma_0^2 - (1 - \widetilde{\alpha}_0)^{-1}]$.[54]

If we can find set of parameters a, b, and k such that Eq. (A1) can be expressed as

$$x^4 + a_1 x^3 + a_2 x^2 + a_3 x + a_4 + (ax + b)^2 = \left(x^2 + \frac{a_1}{2}x + k\right)^2, \tag{A2}$$

Eq. (A1) is solved because Eq. (A2) can be written as

$$\left(x^2 + \frac{a_1}{2}x + k\right)^2 = (ax + b)^2, \tag{A3}$$

where the roots can be found from $x^2 + (a_1/2)x + k = \pm(ax + b)$. Note that the parameters a and b in the Appendix are independent of those in elliptic integrals in the main article.

The unknown parameters a, b, and k can be determined by comparing the left- and right-hand sides in Eq. (A2), thus giving

$$a^2 + a_2 = 2k + a_1^2/4, \tag{A4a}$$

$$2ab + a_3 = ka_1, \tag{A4b}$$

$$b^2 + a_4 = k^2. \tag{A4c}$$

Solving the three equations leads to the following cubic equation for k:

$$k^3 - \frac{a_2}{2}k^2 + \left(\frac{1}{4}a_1 a_3 - a_4\right)k + \frac{1}{2}a_2 a_4 - \frac{1}{8}(a_1^2 a_4 + a_3^2) = 0. \tag{A5}$$

Once k is obtained, a and b can be found from Eqs. (A4a) and (A4c), respectively, where $a = \sqrt{2k + a_1^2/4 - a_2}$ and $b = \sqrt{k^2 - a_4}$ are the solutions.

Equation (A5) can be simply written as

$$y^3 + b_1 y^2 + b_2 y + b_3 = 0, \tag{A6}$$

where $b_1 = -a_2/2$, $b_2 = a_1 a_3/4 - a_4$, and $b_3 = a_2 a_4/2 - (a_1^2 a_4 + a_3^2)/8$.

By setting $y = z - b_1/3$, Eq. (A6) becomes the depressed cubic equation,

$$z^3 + c_2 z + c_3 = 0, \tag{A7}$$

where $c_2 = b_2 - b_1^2/3$ and $c_3 = 2b_1^3/27 - b_1 b_2/3 + b_3$.

Substituting $z = u + v$ into Eq. (A7) yields

$$u^3 + v^3 + (3uv + c_2)(u + v) + c_3 = 0, \tag{A8}$$

Let $3uv + c_2 = 0$, then $v = -c_2/3u$. Inputting v into Eq. (A8) gives

$$u^6 + c_3 u^3 - \frac{1}{27}c_2^3 = 0, \tag{A9}$$

where $u^3 = 0.5(-c_3 \pm \sqrt{c_3^2 + (4/27)c_2^3})$.

If u_1 denotes any of cubic roots of Eq. (A9), the three roots are u_1, ωu_1, and $\omega^2 u_1$, where $\omega = e^{i2\pi/3}$ is the cubic root of unity. The corresponding values of v are $-b_2/3u_1$, $-b_2/3\omega u_1$, and $-b_2/3\omega^2 u_1$, respectively. If $-b_2/3u_1$ is denoted by v_1, the three roots of Eq. (A7) can be expressed as $z_1 = u_1 + v_1$, $z_2 = \omega u_1 + \omega^2 v_1$, $z_3 = \omega^2 u_1 + \omega v_1$.

Thus, Eq. (A4) is solved, and subsequently all roots of Eq. (A1) can be obtained. With some substitutions, the critical values of $\widetilde{x}$ in Eq. (11) can be eventually found as

$$\widetilde{x}_{max} = \frac{1}{2}\left[a - \frac{a_1}{2} - \sqrt{\left(\frac{a_1}{2} - a\right)^2 - 4(k_1 - b)}\right], \tag{A10a}$$

$$\widetilde{x}_{min} = \frac{1}{2}\left[a - \frac{a_1}{2} - \sqrt{\left(\frac{a_1}{2} - a\right)^2 - 4(k_3 - b)}\right], \tag{A10b}$$

where a and b in Eq. (A10a) are determined by

$$k_1 = -\frac{b_1}{3} + \sqrt[3]{\frac{1}{2}\left(-c_3 + \sqrt{c_3^2 + \frac{4}{27}c_2^3}\right)} + \sqrt[3]{\frac{1}{2}\left(-c_3 - \sqrt{c_3^2 + \frac{4}{27}c_2^3}\right)},$$

while a and b in Eq. (A10b) are determined by

$$k_3 = -\frac{b_1}{3} + \omega^2\sqrt[3]{\frac{1}{2}\left(-c_3 + \sqrt{c_3^2 + \frac{4}{27}c_2^3}\right)} + \omega\sqrt[3]{\frac{1}{2}\left(-c_3 - \sqrt{c_3^2 + \frac{4}{27}c_2^3}\right)}.$$

[1] G. A. Mourou, T. Tajima, and S. V. Bulanov, Rev. Mod. Phys. **78**, 309 (2006).
[2] E. Esarey, C. B. Schroeder, and W. P. Leemans, Rev. Mod. Phys. **81**, 1229 (2009).
[3] C. Joshi and V. Malka, New J. Phys. **12**, 045003 (2010).
[4] R. Bingham, J. T. Mendonça, and P. K. Shukla, Plasma Phys. Controlled Fusion **46**, R1 (2004).
[5] A. V. Borovsky, A. L. Galkin, O. B. Shiryaev, and T. Auguste, *Laser Physics at Relativistic Intensities* (Springer, New York, 2003).
[6] U. Teubner and P. Gibbon, Rev. Mod. Phys. **81**, 445 (2009).
[7] T. Baeva, S. Gordienko, and A. Pukhov, Phys. Rev. E **74**, 046404 (2006).
[8] C. Winterfeldt, C. Spielmann, and G. Gerber, Rev. Mod. Phys. **80**, 117 (2008).
[9] A.-T. Le, R. D. Picca, P. D. Fainstein, D. A. Telnov, M. Lein, and C. D. Lin, J. Phys. B **41**, 081002 (2008).
[10] M. Lewenstein, Ph. Balcou, M. Yu. Ivanov, A. L'Huillier, and P. B. Corkum, Phys. Rev. A **49**, 2117 (1994).
[11] F. Krausz and M. Ivanov, Rev. Mod. Phys. **81**, 163 (2009).
[12] A. Scrinzi, M. Y. Ivanov, R. Kienberger, and D. M. Villeneuve, J. Phys. B **39**, R1 (2006).
[13] P. Agostini and L. F. DiMauro, Rep. Prog. Phys. **67**, 813 (2004).
[14] A. Rousse, K. T. Phuoc, R. Shah, A. Pukhov, E. Lefebvre, V. Malka, S. Kiselev, F. Burgy, J.-P. Rousseau, D. Umstadter, and D. Hulin, Phys. Rev. Lett. **93**, 135005 (2004).
[15] R. F. Service, Science **298**, 1356 (2002).

[16] I. Blumenfeld, C. E. Clayton, F.-J. Decker, M. J. Hogan, C. Huang, R. Ischebeck, R. Iverson, C. Joshi, T. Katsouleas, N. Kirby, W. Lu, K. A. Marsh, W. B. Mori, P. Muggli, E. Oz, R. H. Siemann, D. Walz, and M. Zhou, Nature (London) **445**, 741 (2007).

[17] S. P. D. Mangles, C. D. Murphy, Z. Najmudin, A. G. R. Thomas, J. L. Collier, A. E. Dangor, E. J. Divall, P. S. Foster, J. G. Gallacher, C. J. Hooker, D. A. Jaroszynski, A. J. Langley, W. B. Mori, P. A. Norreys, F. S. Tsung, R. Viskup, B. R. Walton, and K. Krushelnick, Nature (London) **431**, 535 (2004).

[18] C. G. R. Geddes, C. Toth, J. van Tilborg, E. Esarey, C. B. Schroeder, D. Bruhwiler, C. Nieter, J. Cary, and W. P. Leemans, Nature (London) **431**, 538 (2004).

[19] V. Malka, S. Fritzler, E. Lefebvre, M.-M. Aleonard, F. Burgy, J.-P. Chambaret, J.-F. Chemin, K. Krushelnick, G. Malka, S. P. D. Mangles, Z. Najmudin, M. Pittman, J.-P. Rousseau, J.-N. Scheurer, B. Walton, and A. E. Dangor, Science **298**, 1596 (2002).

[20] M. Conte and W. W. Mackay, *An Introduction to the Physics of Particle Accelerators* (World Scientific, Singapore, 1991).

[21] I. Kostyukov, A. Pukhov, and S. Kiselev, Phys. Plasmas **11**, 5256 (2004).

[22] W. Lu, C. Juang, M. Zhou, M. Tzoufras, F. S. Tsung, W. B. Mori, and T. Katsouleas, Phys. Plasmas **13**, 056709 (2006).

[23] Y. Glinec, J. Faure, A. Lifschitz, J. M. Vieira, R. A. Fonseca, L. O. Silva, and V. Malka, Europhys. Lett. **81**, 64001 (2008).

[24] N. Kumar and V. K. Tripathi, Europhys. Lett. **75**, 260 (2006).

[25] E. Esarey, B. A. Shadwick, P. Catravas, and W. P. Leemans, Phys. Rev. E **65**, 056505 (2002).

[26] A. G. R. Thomas, Phys. Plasmas **17**, 056708 (2010).

[27] F. Albert, R. Shah, K. T. Phuoc, R. Fitour, F. Burgy, J.-P. Rousseau, A. Tafzi, D. Douillet, T. Lefrou, and A. Rousse, Phys. Rev. E **77**, 056402 (2008).

[28] K. Ta Phuoc, E. Esarey, V. Leurent, E. Cormier-Michel, C. G. R. Geddes, C. B. Schroeder, A. Rousse, and W. P. Leemans, Phys. Plasmas **15**, 063102 (2008).

[29] K. Németh, B. Shen, Y. Li, H. Shang, R. Crowell, K. C. Harkay, and J. R. Cary, Phys. Rev. Lett. **100**, 095002 (2008).

[30] K. T. Phuoc, F. Burgy, J.-P. Rousseau, V. Malka, A. Rousse, R. Shah, D. Umstadter, A. Pukhov, and S. Kiselev, Phys. Plasmas **12**, 023101 (2005).

[31] A. G. Khachatryan, F. A. van Goor, and K.-J. Boller, New J. Phys. **10**, 083043 (2008).

[32] F. Albert, K. T. Phuoc, R. Shah, S. Corde, R. Fitour, A. Tafzi, F. Burgy, D. Douillet, T. Lefrou, and A. Rousse, Plasma Phys. Controlled Fusion **50**, 124008 (2008).

[33] S. Kneip, S. R. Nagel, C. Bellei, N. Bourgeois, A. E. Dangor, A. Gopal, R. Heathcote, S. P. D. Mangles, J. R. Marquès, A. Maksimchuk, P. M. Nilson, K. T. Phuoc, S. Reed, M. Tzoufras, F. S. Tsung, L. Willingale, W. B. Mori, A. Rousse, K. Krushelnick, and Z. Najmudin, Phys. Rev. Lett. **100**, 105006 (2008).

[34] A. Rousse, K. T. Phhuoc, R. Shah, R. Fitour, and F. Albert, Eur. Phys. J. D **45**, 391 (2007).

[35] S. Kiselev, A. Pukhov, and I. Kostyukov, Phys. Rev. Lett. **93**, 135004 (2004).

[36] J. D. Jackson, *Classical Electrodynamics* (Wiley, New York, 1975).

[37] C. M. Wang and J. P. Goedbloed, J. Phys. D **41**, 085203 (2008).

[38] D. H. Froula, L. Divol, P. Davis, J. P. Palastro, P. Michel, V. Leurent, S. H. Glenzer, B. B. Pollock, and G. Tynan, Plasma Phys. Controlled Fusion **51**, 024009 (2009).

[39] N. Najmudin, M. Tatarakis, A. Pukhov, E. L. Clark, R. J. Clark, A. E. Dangor, J. Faure, V. Malka, D. Neely, M. I. K. Santala, and K. Krushelnick, Phys. Rev. Lett. **87**, 215004 (2001).

[40] G. Shvets, N. J. Fisch, and J.-M. Rax, Phys. Rev. E **65**, 046403 (2002).

[41] S. Ali, J. R. Davies, and J. T. Mendonca, Phys. Rev. Lett. **105**, 035001 (2010).

[42] A. K. Upadhyay and P. Jha, Phys. Plasmas **15**, 093101 (2008).

[43] J. A. Stamper, J. M. Dawson, K. Papadopoulos, R. N. Sudan, S. O. Dean, and E. A. Mclean, Phys. Rev. Lett. **26**, 1012 (1971).

[44] J. P. Knauer, O. V. Gotchev, P. Y. Chang, D. D. Meyerhofer, O. Polomarov, R. Betti, J. A. Frenje, C. K. Li, M. J.-E. Manuel, R. D. Petrasso, J. R. Rygg, and F. H. Séguin, Phys. Plasmas **17**, 056318 (2010).

[45] S. Takeuchi, Phys. Rev. E **66**, 037402 (2002).

[46] I. S. Gradshteyn and I. M. Ryzhik, *Table of Integrals, Series, and Products* (Academic, San Diego, 1980), p. 904.

[47] G. A. Korn and T. M. Korn, *Mathematical Handbook for Scientists and Engineers* (McGraw-Hill, New York, 1961), p. 732.

[48] T. Kiyoshi, A. Otsuka, M. Kosuge, M. Yuyama, H. Nagai, and F. Matsumoto, Fusion Eng. Des. **81**, 2411 (2006).

[49] H. J. Schneider-Muntau, J. Toth, and H. W. Weijers, IEEE Trans. Appl. Supercond. **14**, 1245 (2004).

[50] *High Magnetic Fields: Science and Technology*, Vol. 1, edited by F. Herlach and N. Miura (World Scientific, New Jersey, 2003): (a) for limit of resistive magnets, p. 138, (b) for limit of hybrid magnet, p. 149, (c) for controlled waveform magnets, pp. 153–201.

[51] *Current Trends in International Fusion Research*, edited by E. Panarella (NRC Research Press, Ontario, Canada, 2001), p. 273.

[52] *High Magnetic Fields*, edited by H. J. Schneider-Muntau (World Scientific, Singapore, 1997), p. 363.

[53] K. Kindo, Physica B **294–295**, 585 (2001).

[54] R. B. King, *Beyond the Quartic Equation* (Birkhäuser, Boston, 2009), Chap. 5.